14329

ANALYSIS OF THE EFFECTS OF EXHAUST PLACEMENT ON THE THERMAL SIGNATURE OF A CONCEPT VEHICLE

A report written at

US ARMY TACOM

and submitted to

KETTERING UNIVERSITY

MECH-522

Prof. Webster

by

ERIK POLSEN

Summer 2004

Report Documentation Page

Form Approved
OMB No. 0704-0188

1. REPORT DATE	2. REPORT TYPE	3. DATES COVERED
21 JUN 2004	**N/A**	**-**

4. TITLE AND SUBTITLE	5a. CONTRACT NUMBER
Analysis of the Effects of Exhaust Placement on the Thermal Signature of a Concept Vehicle	5b. GRANT NUMBER
	5c. PROGRAM ELEMENT NUMBER
6. AUTHOR(S) **Erik Polsen**	5d. PROJECT NUMBER
	5e. TASK NUMBER
	5f. WORK UNIT NUMBER
7. PERFORMING ORGANIZATION NAME(S) AND ADDRESS(ES) **USA TACOM 6501 E 11 Mile Road Warren, MI 48397-5000**	8. PERFORMING ORGANIZATION REPORT NUMBER **14329**
9. SPONSORING/MONITORING AGENCY NAME(S) AND ADDRESS(ES)	10. SPONSOR/MONITOR'S ACRONYM(S) **TACOM TARDEC**
	11. SPONSOR/MONITOR'S REPORT NUMBER(S)

12. DISTRIBUTION/AVAILABILITY STATEMENT
Approved for public release, distribution unlimited

13. SUPPLEMENTARY NOTES
A report written at US ARMY TACOM and submitted to Kettering University MECH-522 Prof. Webster

14. ABSTRACT

15. SUBJECT TERMS

16. SECURITY CLASSIFICATION OF:			17. LIMITATION OF ABSTRACT	18. NUMBER OF PAGES	19a. NAME OF RESPONSIBLE PERSON
a. REPORT **unclassified**	b. ABSTRACT **unclassified**	c. THIS PAGE **unclassified**	**SAR**	**50**	

I. INTRODUCTION

This chapter will present the initial necessary information needed to understand the following chapters. The text below provides an overall understanding of the problem topic first, and then includes pertinent information regarding the background of the posed problem. Next, the criteria and parameters imposed will be identified, followed by the methodology used in solving the problem. Finally, the primary purposes and a brief overview of the report will be discussed.

Problem Topic

Due to the high cost of modifying vehicles after production in order to reduce the thermal signature, this report evaluates the effects of the placement of the vehicle's exhaust outlet on the overall thermal signature during the conceptual phase. In the past, the lack of regard for the thermal signature during the design of a ground vehicle often led to millions of dollars spent to minimize the thermal signature post-production. Integrating thermal management into the design process at the concept level allows for a better overall system that combines the best of lethality, mobility, and survivability. By designing a better overall system the Tank-Automotive Research, Development, and Engineering Center (TARDEC) provides the soldier with superior war-fighting capabilities.

Background

The need for thermal signature management has become increasingly important over the past few years due to the advancements in electronics technology. With these advancements came a dramatic decrease in the price of military sensors, such as Forward Looking Infrared (FLIR) sensors, giving less wealthy, potential threat nations the ability to afford them. Thermal or IR signature management has become just as important as how a vehicle looks visually, since these nations now have a detection capability previously unavailable to them. A vehicle could be deemed "invisible" to the naked eye, but without IR treatment, once viewed through a FLIR sensor, the vehicle could be detected and targeted easily (see Figure 1).

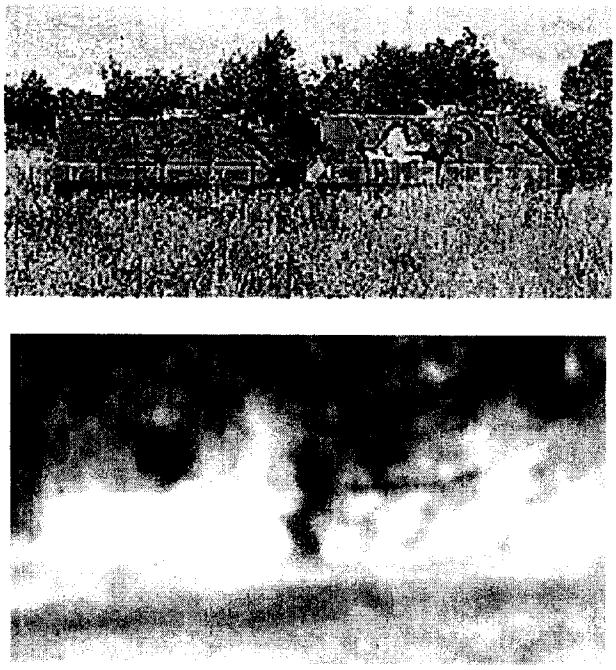

Figure 1. M-113 visible and IR images. Both vehicles are considered adequately camouflaged in the visible domain (top) when at range, but since the vehicle on the left does not have thermal treatment it can be seen easily in the IR domain (bottom).

In the past, the thermal signature of a vehicle was often ignored during the design phase. In the interest of keeping cost and complexity down, the exhaust outlet for military vehicles was often located as close to the engine as possible so as to keep from intruding upon the crew compartment and creating problems with space claims for other systems. This often meant that the exhaust exited the front portion of the hull either from the top or the side of the vehicle, leaving the hot exhaust plume free to heat a large portion of the vehicle as it moved through the battlefield. At the time this was not a problem since IR sensors were very expensive and most countries could not afford to use them, but as the threat becomes more of an issue the older systems will need to be thermally treated. Unfortunately, treatments for the systems to minimize their thermal signatures after production are more costly than a more effective design from the beginning. With the increasing IR threat and the realization that the signature aspect of a vehicle should not be left as an "add-on kit," signature management is becoming more integrated with the initial designs for Army ground vehicles.

With consideration for the thermal signature of the vehicle integrated into the concept phase, basic methods to minimize the signature can be applied before relying on expensive treatments. The first of these methods is to position the exhaust outlet in such a way that it is hidden from enemy sensors a majority of the time (a line-of-sight problem). By placing the exhaust outlet at the rear of the vehicle, it is hidden from both ground and aerial thermal sensors as the vehicle moves through the battlefield (given that the enemy has not been able to gain a position to the rear of the formation). Other than line-of-sight, great care is taken to ensure that the hot exhaust gases have very little

interaction with the surrounding terrain or other portions of the vehicle. If the exhaust is allowed to heat other objects through convection the thermal signature that the vehicle creates becomes much larger, making the vehicle easier to target at long ranges. Both of these methods, while very basic, drastically improve the survivability of a ground system when encountered with an IR threat.

Unfortunately there is not one general solution that will work with every ground vehicle. Size, cost, and configuration constraints of a system limit where the exhaust can exit the vehicle. While a rear exit exhaust works well with an M1A2 Abrams Battle Tank, routing the exhaust to the rear of the vehicle, where the engine is located at the front, requires a large volume of the crew compartment to be sacrificed in order to keep the exhaust ballisticly protected. Likewise, an exhaust outlet directed towards the ground may impinge on the terrain below leaving a thermal trail, while a swept back design may impinge on the vehicle itself once it is in motion. A vehicle's inherent geometry may also effect plume impingement. Regardless of the vehicle being designed, each logical exhaust location needs to be studied with various configurations to ensure that the thermal signature of the system is minimized before production.

Criteria and Parameter Restrictions

For evaluating the effects of the exhaust outlet placement on the thermal signature of the given concept vehicle, the author has determined six criteria and parameter restrictions in order for the comparison of the simulations to be considered adequate. The thermal simulations must:

1. Utilize a concept vehicle that resembles a likely future force vehicle.
2. Use a woodland weather and terrain scenario during the summer.

3. Include two vehicle scenarios: Midday vehicle stationary and engine idle, and Midday vehicle dynamic at 20 mph.

4. Include three exhaust outlet placements for each of the scenarios: Top, side, and rear exiting.

5. Allow for a comparison of the exhaust variants using the RSSΔT detection algorithm and Probability of Detection (Pd) experiments.

6. Include an analysis of the variants in both the 3-5 and 8-12 micron bands, where the lower the RSSΔT and Pd values are the better the design is from a thermal signature standpoint.

These criteria are valid because they directly relate to typical specifications set forth by US Army TARDEC. Also, meeting these criteria would insure that the proper exhaust placement would be used if the concept vehicle were ever fielded.

Methodology

Development of the solution to the problem presented, followed several specific steps. Identifying the problem and how it impacts the organization was the first step, followed by the selection of a suitable concept vehicle. Next, research of the possible exhaust routings through the concept vehicle was conducted to ensure that there was adequate space to meet the three exhaust outlet scenarios. The three vehicle variants were then designed and meshed using independent CAD and surface meshing tools. Thermal signature solutions were then created using a combination of computational fluid dynamics (CFD) and heat transfer packages. Finally, virtual field-testing was conducted, comparing the three exhaust variants in various backgrounds to verify what a lower thermal signature actually bought the soldier.

Design and analysis of the exhaust placement study was accompanied by several data sources throughout the process. Data sources that were at the author's disposal are as follows: direct observations of field-tests, technical publications from various sources,

academic texts, Pro Engineer (CAD), Eclectic (meshing tool), Fluent (CFD), Multi-service Electro-optical Signature Code (MuSES) 7.0 used for thermal modeling, Paint the Night (Pd Software), CameoSim (visual and thermal scene generator), and other engineers with experience in the field.

Primary Purpose

This report represents the results of the investigation into the effects of the placement of the exhaust outlet of a concept vehicle on the overall thermal signature and its probability of detection.

Overview

The next chapter presents information on the modeling of the concept vehicle, including solid modeling, transformation of the solid model into a surface model, and the meshing of the surface model for use by Fluent and MuSES. Chapter III covers the simulation involved in the project, including an in-depth look at the thermal solver package MuSES from a numerical methods standpoint. The CFD solutions for the exhaust plumes using Fluent, numerical methods that are utilized within MuSES and how they are applied, thermal solutions for the vehicles using MuSES, and the Pd results from Paint the Night (PTN) are all included in Chapter III. Finally, Chapter IV presents the conclusions and recommendations of the author, for this investigation, based on the criteria and parameters already specified.

II. MODELING

This chapter will present the information regarding the computer modeling of the concept vehicle and associated exhaust placements. In the text below, the reasoning behind the selection of the concept vehicle will be discussed. Exhaust exit locations and possible routings will be covered second, followed by all of modifications made to the solid model to prepare the geometry for surface mesh. Finally, all issues dealing with the surface meshing of the vehicle variants will conclude the chapter.

Platform Selection

The selection of a test platform was primarily driven by the U.S. Army's drive towards lighter combat vehicles, also known as Future Combat Systems (FCS). Since the future of combat vehicles is moving towards lighter vehicles (accomplished by using less massive armor) any vehicle with heavy armor protection was not considered for this study. In order to be able to share this study with other organizations, the vehicle concept that was selected from TARDEC's Advanced Concept Team represented a surrogate future platform but did not have a great deal of detail. While not very detailed, the wheeled vehicle concept that was selected (see Figure 2) provided an appropriate platform based on the given criteria.

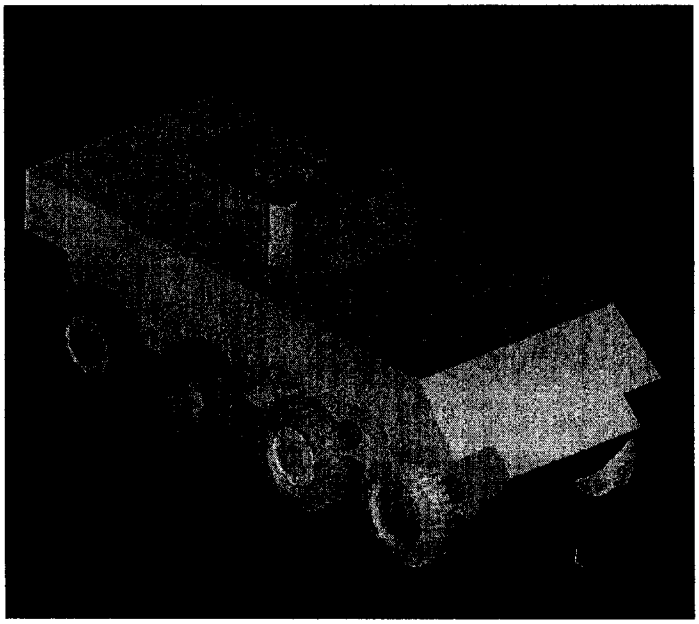

Figure 2. Concept vehicle solid model.

With the concept vehicle selected, the next step was to investigate exhaust routings (consisting of engine cooling air and engine exhaust) for each of the three variants. Since this concept was designed with the engine located at the front of the vehicle, both the top and side exhaust outlet routings allowed for the ducting to be kept entirely within the engine compartment. As shown in Figures 3a and 3b, the top outlet was located just to the rear of the air intake while the side outlet was located towards the front of the upper glacis. Although there was enough space to route the ducting to the rear of the vehicle from engine, a great deal of volume in the crew compartment was given up. The ducting for the rear exhaust outlet routed inside the hull, down the right sponson (area overhanging the wheels) to the upper center portion of the rear of the vehicle (see Figure 3c). In order to keep each variant similar, the same size ballistic grille was used for each of the outlets on the outside of the hull.

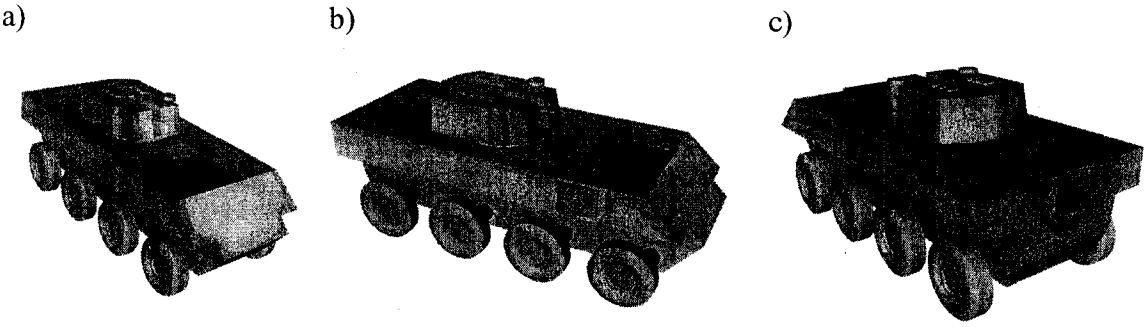

Figure 3. Exhaust outlet locations.

Finally, the engine and powertrain configuration for the concept was investigated in order to obtain the information needed to develop accurate plume and heat models. The powertrain for the concept vehicle consisted of a Detroit Diesel, 24-valve, turbocharged V-6 (182.7 kW @ 2700 rpm) that was connected directly to a generator. Electrical power from the generator powered individual in-hub motors for each wheel. Thus, while the vehicle was in motion the engine would run at a constant speed to keep the system operating at its most efficient point. Based on the previous information, temperature and flow parameters for the exhaust were selected based on past experience with such a setup (Idle: 1200 cfm @ 110 °C; 20 mph: 3880 cfm @ 499 °C). Application of the thermal energy given off by the in-hub motors and the engine will be discussed in the next chapter.

Pre-Processing

With the geometry for the model and the characteristics of the exhaust plume known, the next step was to modify the geometry in preparation for the CFD and thermal solvers. Since the main concern of the study was the thermal signature of the vehicle in relation to the exhaust placement, the tires were modified to reduce the computational

complexity without affecting the desired output. As shown in Figure 4, the tread of the tires was removed and replaced with a flat surface in order to reduce the number of facets in the model, which made the meshing process much easier. The rest of the geometry for the tires was left unchanged.

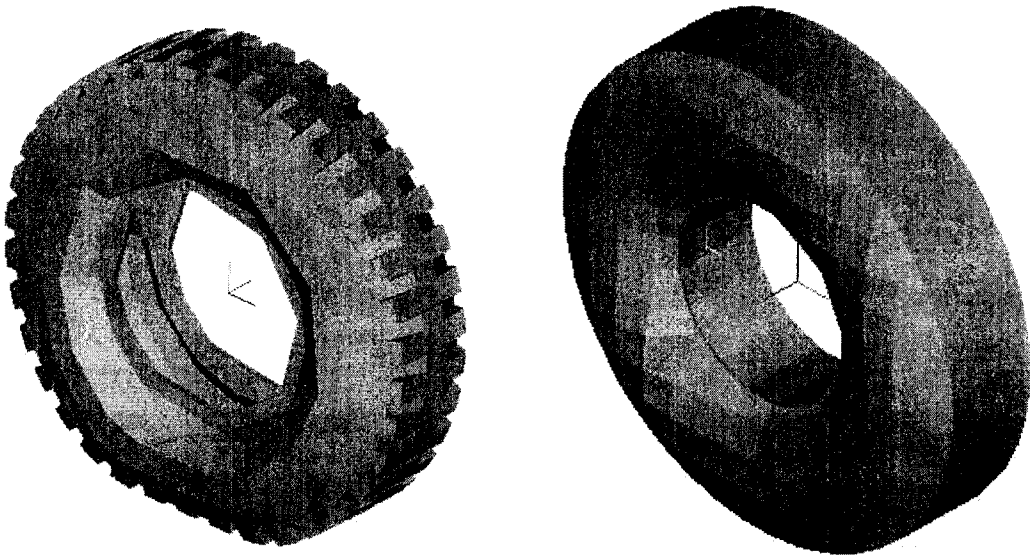

Figure 4. Tire comparison. The original tire is shown on the left, while the tire without the tread that was used in the study is shown on the right.

Other than the wheels, a turret ring needed to be added to the geometry to allow for proper heat transfer. The original vehicle geometry did not include a turret ring and thus the turret was floating above the hull (see Figure 5). By adding a ring of material between the turret and the hull the two components were then connected. Without connecting the turret to the hull there would have been zero nodes between them, thus no thermal conduction could have taken place in that location. This completed the modifications to the solid geometry before proceeding to the surface meshing.

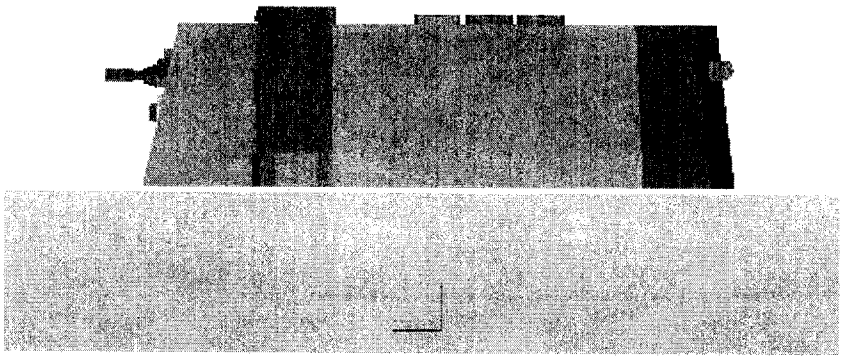

Figure 5. Missing turret ring. This side view shows the gap between the hull and the turret before the turret ring was added.

With the solid geometry completed, the files were exported for use in a surface-meshing program. The files were exported from Pro Engineer using a Stereo Lithography file format (*.stl) so that they could be imported into Eclectic, a program developed by Jack Jones at US Army TACOM. With the geometry imported into Eclectic, a user-defined surface-mesh was applied to each surface (see Figure 6). The mesh for the concept vehicle was sized so that there was minimal distortion on the curved surfaces of the vehicle, such as the tire sidewalls. Also, the mesh was sized as large as possible to minimize computational time, yet small enough to minimize any "grain" effect when viewed at range in any of the post processor packages. With the meshing completed each of the files were exported in a Wavefront (*.obj) file format so that the surface meshed geometry could be imported into Fluent and MuSES 7.0.

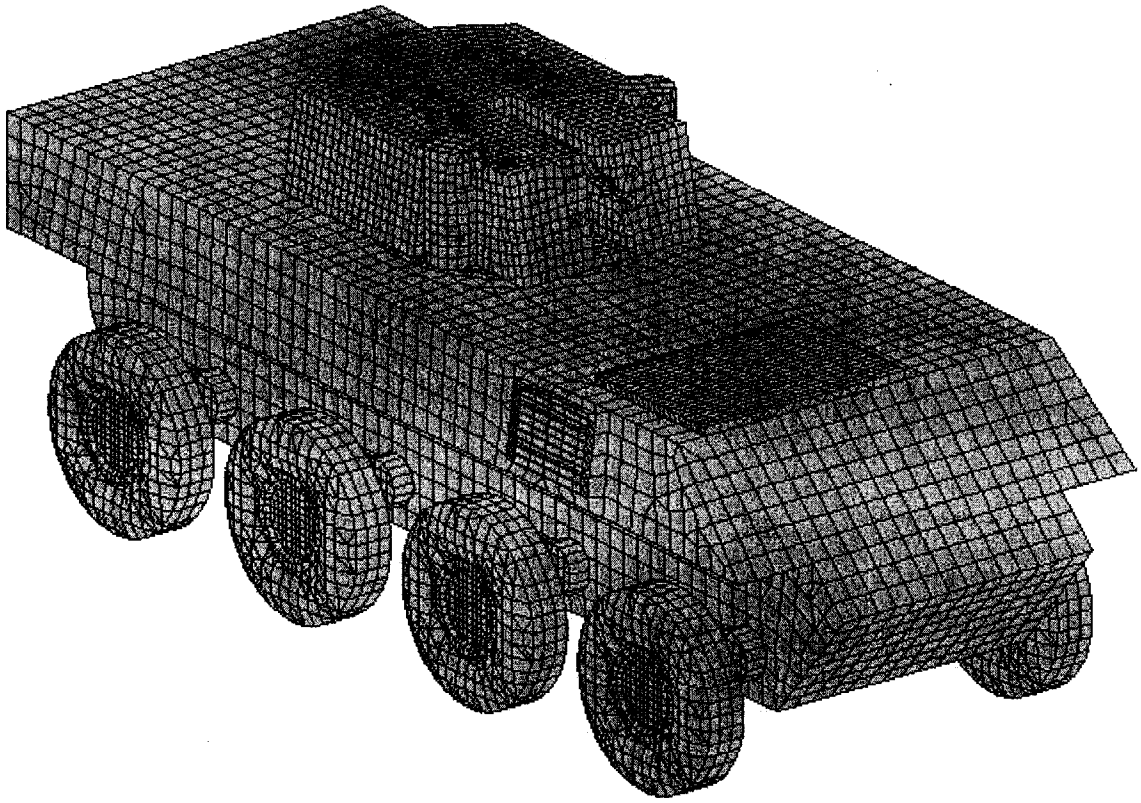

Figure 6. Surface mesh for concept vehicle. The mesh above is for the side exhaust variant.

III. SIMULATION

This chapter covers the fluid dynamics, thermal, and probability of detection simulations used in this project. The exhaust plume generation for each of the variants using CFD software is discussed first. Next, an in-depth look at the numerical methods used by MuSES to solve heat transfer problems is presented. Finally, the thermal analysis of the variants is covered, followed by the use of the probability-of-detection experiments. Due to the many simulation aspects of this project, some of the work was done by individuals other than the author and are noted in the appropriate sections.

Exhaust Plume Generation

The impingement of the exhaust plumes on the vehicle hulls was the main focus for this study, so the plume characteristics were handled first. Since MuSES does not support CFD directly, the exhaust plume for the vehicles needed to be modeled using a separate software package. Rob Smith of ThermoAnalytics Inc. (TAI) selected Fluent as the CFD software for this analysis and handled this portion of the study. Programmers at TAI (also the company that created MuSES) also added a new segment of code that allowed the results from the CFD simulation to be input into MuSES for the thermal solution.

Using Fluent, the plume was modeled with the supplied vehicle and engine parameters from TARDEC. The boundary conditions used for generating the steady-state exhaust plume for both the idle and 20 mph scenarios are shown in Table 1. Also, a

preliminary MuSES thermal model was run for each vehicle (without the effects of the exhaust) to obtain initial surface temperatures on the hull. The surface temperatures were then used as wall boundary conditions on the hull in the CFD model, and a multi-step process was implemented which will be explained in the Thermal Signature Simulation section. Figure 7 shows the CFD domain consisting of 509,051 prism and tetrahedral elements. High concentrations of elements were placed around the exhaust outlet areas gradually expanding to the outer boundary regions. Forward motion was simulation by assigning an inlet velocity at the front of the domain and a moving ground plane. The standard k-e solver was used to model the turbulence and the walls were modeled using wall functions. In solving the model, special attention was paid to the mesh height at the walls. The Y* and Y+ values (measurements of boundary layer thickness) had to be in the correct range in order to properly capture the physics near the wall.

Table 1. Boundary conditions for exhaust plume generation.

	Idle	20 Mph Forward
Speed	-none-	20 mph
Exhaust temperature	110 Celsius	499 Celsius
Volumetric exhaust flow	1200 cfm	3880 cfm

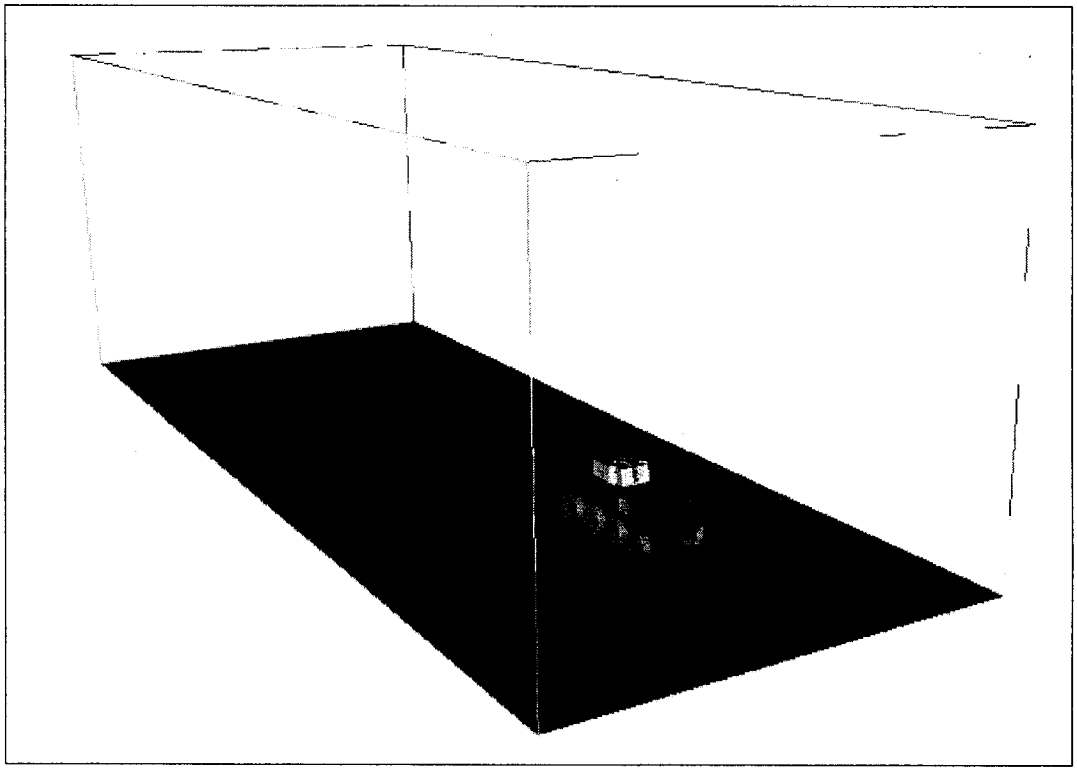

Figure 7. CFD domain for the exhaust plume generation.

With the domain and all of the boundary conditions input, the convection coefficients and the geometry for each of the exhaust plumes were calculated. As shown in Figure 8, at idle the exhaust plume exiting from the top of the vehicle impinges on the turret of the vehicle. The impingement of the top exhaust plume was due to the ballistic grill fins being angled towards the rear of the vehicle, while the side and rear variants were angled down. Figure 9 illustrates the exhaust plumes from the 20 mph simulation. Due to the airflow across the vehicle at 20 mph, the plumes were all noticeably swept towards the rear of the vehicle. The top exhaust plume engulfed the turret and much of the top of the vehicle, while the side exhaust plume impinged on the side glacis of the

vehicle. All of this impingement meant that the plume would definitely affect the thermal signature of the vehicle in the contact areas.

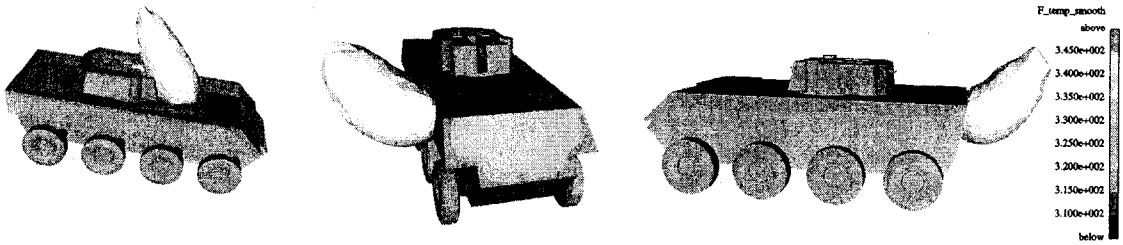

Figure 8. Idle exhaust plumes with 325 Kelvin exhaust isotherms.

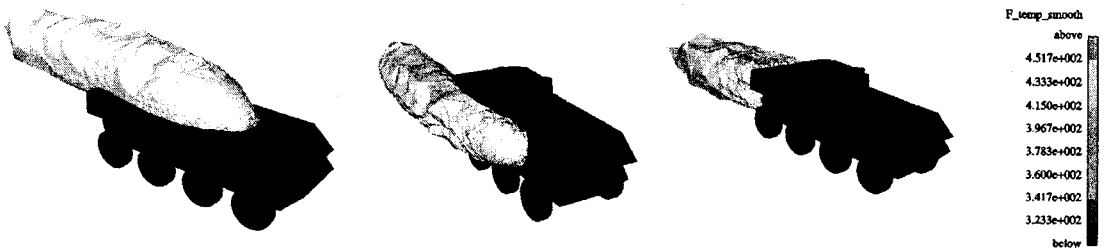

Figure 9. 20 mph exhaust plumes with 325 Kelvin exhaust isotherms.

While the CFD simulations of the top and side exhaust variants illustrated a great deal of impingement on the vehicle, the rear exit exhaust was not clearly the best choice. Looking at Figure 9, the exhaust plume from the rear exit variant is swept back like the others but it is also the width of the vehicle. Looking at the velocity vectors at the rear of the vehicle, the reason for the large cross-sectional plume became very apparent. As the air flows over the vehicle it forms a boundary layer, however once the vehicle profile

drops off sharply the air separates from the surface of the vehicle and forms a low pressure area (see Figure 10). Due to the low pressure area the air within the region swirls and causes recirculation of the exhaust gases exiting the vehicle, thus creating a larger area of impingement. In order to determine which exhaust location would provide the smallest thermal signature, both a thermal analysis and a probability of detection analysis were conducted next.

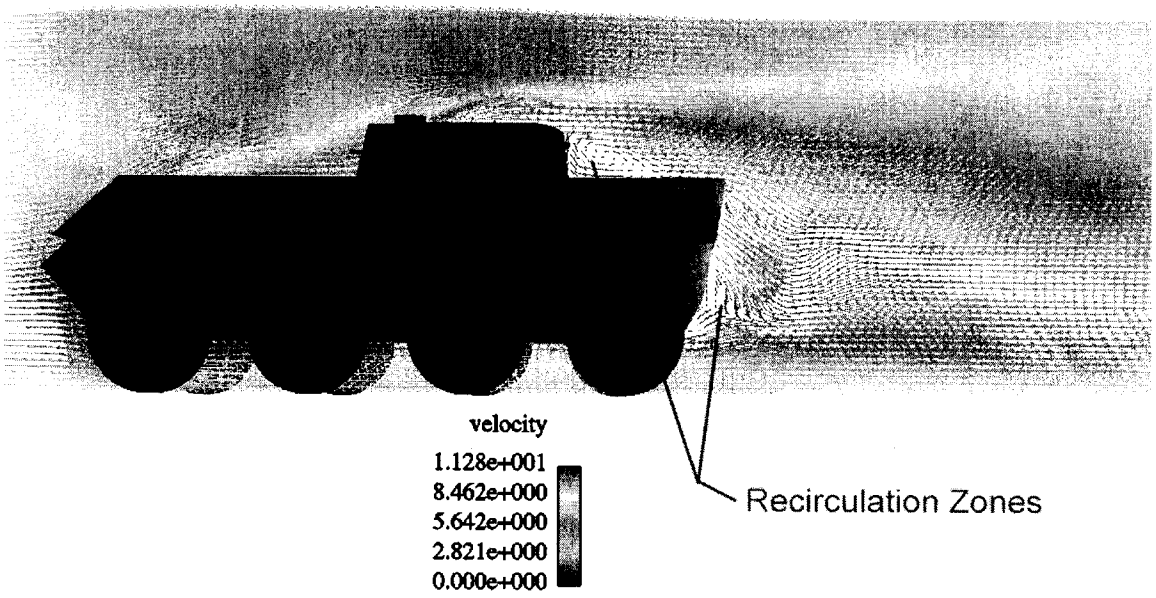

Figure 10. Velocity profile of rear exhaust variant.

Numerical Methods Used by MuSES

Although all simulations included in this study are important, the main tool used for thermal signature simulation was MuSES. The fact that MuSES is the cornerstone in this area of study warrants a closer look at how the software calculates the output values. This section will discuss the numerical methods that are applied to the heat transfer

equations in order to minimize computational time and provide accurate results. Also, the numerical methods that are used within MuSES will be applied to a basic problem (since trying to calculate thousands of nodes from this vehicle study would be cumbersome) to illustrate how everything works.

MuSES performs an energy balance based on the calculations of convection, conduction, and radiation for a given geometry. The geometry of the problem must be discretized into a mesh consisting of triangular and/or quadrilateral elements. The method by which the elements are thermally linked together is automated under user inputs. Environmental effects (solar loads, sky and earth emission, etc.), external convection, and precipitation are all input via a weather file or calculated internally. Also, all temperature and heat load data are input as constants or as functions of time directly by the user.

Each element in the mesh is modeled as two surfaces (front and back) separated by a specified thickness. The individual surfaces then have a thermal node associated with each of them. Each thermal node is associated with the surface and with one-half of the volume that is bounded by the two surfaces (see Figure 11). A single temperature is assumed for the volume that is associated with each thermal node.

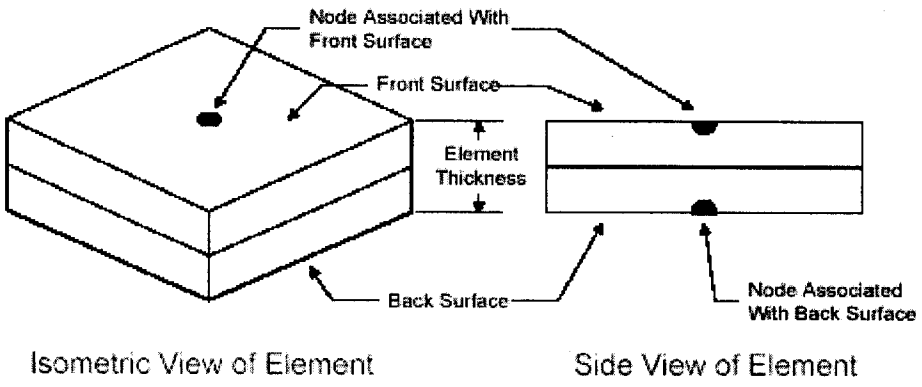

Figure 11. Illustration of the surface node configuration.

The governing equations are then evaluated for each node. Figure 12 is a schematic of a node showing all of the heat transfer modes that are accounted for. The governing equations used for the problem are the transient energy equation, and the net-radiation enclosure equation.

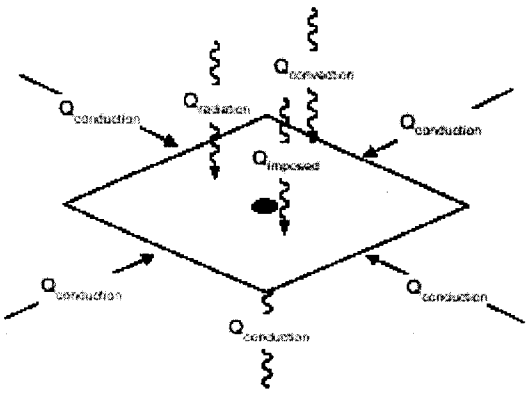

Figure 12. Illustration of all heat transfer modes for each node.

Starting with the transient energy equation for the node shown in Figure 12 yields:

$$\frac{\partial E}{\partial t} = \sum Q \tag{1}$$

Expanding Eqn. (1) results in:

$$mC_p \frac{\partial T}{\partial t} = Q_{convection} + Q_{conduction} + Q_{radiation} + Q_{imposed} \tag{2}$$

where m is the mass of the node, T is the temperature of the node, t is time, and C_p is the specific heat of the material. Each Q term represents a mode of heat transfer, where $Q_{imposed}$ is present to model auxiliary heat transfer such as solar energy or electrical heat generation. Expanding the $Q_{convection}$ and $Q_{conduction}$ terms for the i^{th} node:

$$m_i C_{p_i} \frac{\partial T}{\partial t} = h_i A_i (T_f - T_i) + \sum_{j=1}^{N_{cond}} \left(-k_{ij} A_{ij} \frac{T_i - T_j}{L_{ij}} \right) + Q_{rad_i} + Q_{imp_i} \tag{3}$$

where $\sum_{j=1}^{N_{cond}} \left(-k_{ij} A_{ij} \frac{T_i - T_j}{L_{ij}} \right)$ is the summation of all of the conduction from each node around the i node, h_i is the convection coefficient, A_i is the node surface area exposed to convection, T_f is the temperature of the fluid, k_{ij} is the thermal conductivity of the material, A_{ij} is the area of contact between nodes i and j, and L_{ij} is the geometric distance between nodes i and j. Q_{rad_i} is obtained from the net-radiation enclosure equation for radiation between N diffuse-gray surfaces, written for the i^{th} surface (MuSES v. 7.1 Technical Manual, TAI, 2004):

$$\sum_{j=1}^{N} \left(\frac{\delta_{ij}}{\varepsilon_j} - F_{i-j} \frac{1-\varepsilon_j}{\varepsilon_j} \right) \frac{Q_j}{A_j} = \sum_{j=1}^{N} \sigma F_{i-j} \left(T_i^4 - T_j^4 \right) \tag{4}$$

where ε_j is the emissivity of surface j, F_{i-j} is the view factor from surface i to surface j, σ is the Stephan-Boltzmann constant, A_j is the surface area, and δ_{ij} is the Kronecker delta squared. Solving Eqn. (4) for Q_i (MuSES v. 7.1 Technical Manual, TAI, 2004):

$$Q_i = \frac{\varepsilon_i A_i}{1 - F_{i-i}(1-\varepsilon_i)}\left[\sum_{j=1}^{N}\left((1-\delta_{ij})F_{i-j}\frac{1-\varepsilon_j}{\varepsilon_j}\right)\frac{Q_j}{A_j} + \sum_{j=1}^{N}\sigma F_{i-j}\left(T_i^4 - T_j^4\right)\right] \tag{5}$$

where Q_i is the net radiative loss from the ith surface, and is equal to $-Q_{rad_i}$ in Eqn. (3). Replacing Q_{rad_i} with $-Q_i$ in Eqn. (3) and solving for Q_i results in:

$$Q_i = -m_i C_{p_i}\frac{\partial T_i}{\partial t} + h_i A_i (T_f - T_i) + \sum_{j=1}^{N_{cond}}\left(-k_{ij}A_{ij}\frac{T_i - T_j}{L_{ij}}\right) + Q_{imp_i} \tag{6}$$

For transient solutions MuSES applies the Crank-Nicholson method to Eqn. (5) and (6). Applying this time-averaging, implicit, finite difference scheme to Eqn. (5) and linearizing the T^4 terms yields:

$$Q_i = \frac{\varepsilon_i A_i}{1 - F_{i-i}(1-\varepsilon_i)}\left[\begin{array}{l}\displaystyle\sum_{j=1}^{N}\left((1-\delta_{ij})F_{i-j}\frac{1-\varepsilon_j}{\varepsilon_j}\right)\frac{Q_j}{A_j} \\ \displaystyle + \sum_{j=1}^{N}\sigma F_{i-j}\left(T_i^{n\,2} + T_j^{n\,2}\right)\left(T_i^n + T_j^n\right)\left(\frac{T_i^{n+1} + T_i^n}{2} - \frac{T_j^{n+1} + T_j^n}{2}\right)\end{array}\right] \tag{7}$$

Using the Crank-Nicholson method for Eqn. (6) results in:

$$\begin{aligned} Q_i = {} & -m_i C_{p_i}\frac{\left(T_i^{n+1} - T_i^n\right)}{\Delta t} + h_i A_i\left(\frac{T_f^{n+1} + T_f^n}{2} - \frac{T_i^{n+1} + T_i^n}{2}\right) \\ & + \sum_{j=1}^{N_{cond}}\frac{k_{ij}A_{ij}}{L_{ij}}\left(\frac{T_j^{n+1} + T_j^n}{2} - \frac{T_i^{n+1} + T_i^n}{2}\right) + \frac{Q_{imp_i}^{n+1} + Q_{imp_i}^n}{2} \end{aligned} \tag{8}$$

where n+1 represents the current time step, and n represents the previous time step. Combining Eqn. (7) and (8) yields:

$$
\begin{aligned}
&-m_i C_{p_i}\frac{\left(T_i^{n+1}-T_i^{n}\right)}{\Delta t}+h_i A_i\left(\frac{T_f^{n+1}+T_f^{n}}{2}-\frac{T_i^{n+1}+T_i^{n}}{2}\right)\\
&+\sum_{j=1}^{N_{cond}}\frac{k_{ij}A_{ij}}{L_{ij}}\left(\frac{T_j^{n+1}+T_j^{n}}{2}-\frac{T_i^{n+1}+T_i^{n}}{2}\right)+\frac{Q_{imp_i}^{n+1}+Q_{imp_i}^{n}}{2}\\
&=\frac{\varepsilon_i A_i}{1-F_{i-i}\left(1-\varepsilon_i\right)}\left[\begin{aligned}&\sum_{j=1}^{N}\left(\left(1-\delta_{ij}\right)F_{i-j}\frac{1-\varepsilon_j}{\varepsilon_j}\right)\frac{Q_j}{A_j}\\&+\sum_{j=1}^{N}\sigma F_{i-j}\left(T_i^{n\,2}+T_j^{n\,2}\right)\left(T_i^{n}+T_j^{n}\right)\left(\frac{T_i^{n+1}+T_i^{n}}{2}-\frac{T_j^{n+1}+T_j^{n}}{2}\right)\end{aligned}\right]
\end{aligned}
\tag{9}
$$

Eqn. (9) can then be simplified by multiplying by 2:

$$
\begin{aligned}
&-2m_i C_{p_i}\frac{\left(T_i^{n+1}-T_i^{n}\right)}{\Delta t}+h_i A_i\left(T_f^{n+1}+T_f^{n}-T_i^{n+1}-T_i^{n}\right)\\
&+\sum_{j=1}^{N_{cond}}\frac{k_{ij}A_{ij}}{L_{ij}}\left(T_j^{n+1}+T_j^{n}-T_i^{n+1}-T_i^{n}\right)+Q_{imp_i}^{n+1}+Q_{imp_i}^{n}\\
&=\frac{\varepsilon_i A_i}{1-F_{i-i}\left(1-\varepsilon_i\right)}\left[\begin{aligned}&2\sum_{j=1}^{N}\left(\left(1-\delta_{ij}\right)F_{i-j}\frac{1-\varepsilon_j}{\varepsilon_j}\right)\frac{Q_j}{A_j}\\&+\sum_{j=1}^{N}\sigma F_{i-j}\left(T_i^{n\,2}+T_j^{n\,2}\right)\left(T_i^{n}+T_j^{n}\right)\left(T_i^{n+1}+T_i^{n}-T_j^{n+1}-T_j^{n}\right)\end{aligned}\right]
\end{aligned}
\tag{10}
$$

Solving Eqn. (10) for T_i^{n+1} the final equation for a transient solution is found:

$$
T_i^{n+1}=\frac{\dfrac{2m_i C_{p_i}}{\Delta t}T_i^{n}+\sum_{j=1}^{Ntotal}C_{ij}\left(T_{j,f}^{n+1}+T_{j,f}^{n}-T_i^{n}\right)+Q_{imp_i}^{n+1}+Q_{imp_i}^{n}-\dfrac{2\varepsilon_i A_i}{1-F_{i-i}\left(1-\varepsilon_i\right)}\sum_{j=1}^{N}\left(\left(1-\delta_{ij}\right)F_{i-j}\dfrac{1-\varepsilon_j}{\varepsilon_j}\right)\dfrac{Q_j}{A_j}}{\dfrac{2m_i C_{p_i}}{\Delta t}+\sum_{j=1}^{Ntotal}C_{ij}}
\tag{11}
$$

where C_{ij} is equal to:

$$h_i A_i \qquad \text{(For convection, and } T_f \text{ is used instead of } T_j\text{)} \tag{12a}$$

$$\frac{k_{ij}A_{ij}}{L_{ij}} \qquad \text{(For conduction)} \tag{12b}$$

$$\frac{\varepsilon_i A_i}{1-F_{i-i}\left(1-\varepsilon_i\right)}\sum_{j=1}^{N}\sigma F_{i-j}\left(T_i^{n\,2}+T_j^{n\,2}\right)\left(T_i^{n}+T_j^{n}\right) \qquad \text{(For radiation)} \tag{12c}$$

Eqn. (11) is then used for each node to be solved. MuSES solves these equations using a Gauss-Seidel procedure where the new values are used in the equation as soon as they become available. Convergence is achieved when the greatest nodal temperature difference between the present iteration and the previous iteration is less than an amount specified by the user.

If a steady state solution is desired, then the above equations can be simplified greatly. Starting with Eqn. (9), all occurrences of $\frac{T^{n+1}+T^n}{2}$ can be replaced with T, and the time dependent term can be eliminated to yield:

$$h_i A_i (T_f - T_i) + \sum_{j=1}^{N_{cond}} \frac{k_{ij} A_{ij}}{L_{ij}} (T_j - T_i) + Q_{imp_i} = \frac{\varepsilon_i A_i}{1 - F_{i-i}(1-\varepsilon_i)} \left[\sum_{j=1}^{N} \left((1-\delta_{ij}) F_{i-j} \frac{1-\varepsilon_j}{\varepsilon_j} \right) \frac{Q_j}{A_j} + \sum_{j=1}^{N} \sigma F_{i-j} (T_i^2 + T_j^2)(T_i + T_j)(T_i - T_j) \right] \quad (13)$$

Solving Eqn. (13) for T_i results in:

$$T_i = \frac{\sum_{j=1}^{Ntotal} C_{ij} T_{j,f} + Q_{imp_i} - \frac{\varepsilon_i A_i}{1 - F_{i-i}(1-\varepsilon_i)} \sum_{j=1}^{N} \left((1-\delta_{ij}) F_{i-j} \frac{1-\varepsilon_j}{\varepsilon_j} \right) \frac{Q_j}{A_j}}{\sum_{j=1}^{Ntotal} C_{ij}} \quad (14)$$

where C_{ij} is equal to:

$h_i A_i$ (For convection, and T_f is used instead of T_j) (15a)

$\frac{k_{ij} A_{ij}}{L_{ij}}$ (For conduction) (15b)

$\frac{\varepsilon_i A_i}{1 - F_{i-i}(1-\varepsilon_i)} \sum_{j=1}^{N} \sigma F_{i-j} (T_i^2 + T_j^2)(T_i + T_j)$ (For radiation) (15c)

Once again a Gauss-Seidel approach is used to solve the temperature equations for the various nodes.

A very brief example will now be investigated using the steady state approach that is coded into MuSES. While a whole vehicle was not solved here analytically due to the shear size of the problem, the example does lend itself to the particular scenario that is the focus of this study. Figure 13 illustrates the geometry used for this example. The geometry represents a piece of armor that is 0.0254 m thick and 0.5 m square (distance between nodes is 0.1 m). Assuming that the rear of the plate and the outer edges are all insulated, the frontal nodes (shown) are the only ones having any interaction with the surroundings. Let nodes 2-5, 8-10, 13-15, 19, 20, & 25 have interaction with 773°K exhaust gas ($h = 600\ W/m^2K$), and all of the remaining nodes have interaction with 294°K ambient air ($h = 150\ W/m^2K$). Also, let each node have a solar loading value of $900\ W/m^2$.

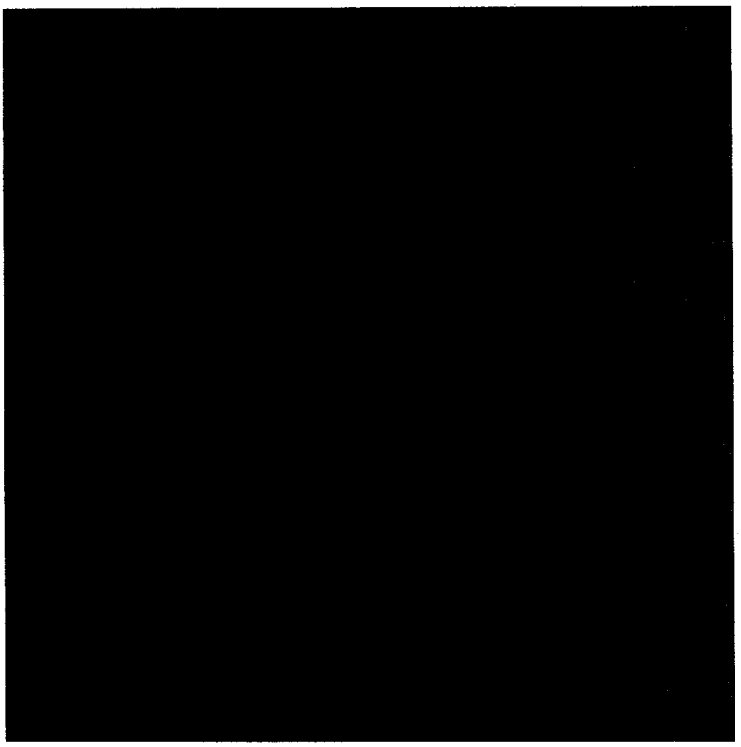

Figure 13. Geometry for example problem.

Since radiation is not considered in this example, Eqn. (14) becomes:

$$T_i = \frac{h_i A_i T_f + \sum_{j=1}^{Ncond} \frac{k_{ij} A_{ij}}{L_{ij}} T_j + Q_{imp_i}}{h_i A_i + \sum_{j=1}^{Ncond} \frac{k_{ij} A_{ij}}{L_{ij}}} \tag{16}$$

where Q_{imp_i} = 900 (W/m^2) x A_i, L_{ij} = 0.1 (m), and k_{ij} = 60.5 (W/m K). Setting up the other parameters for the first five nodes yields:

$$A_1 = A_2 = A_3 = A_4 = A_5 = (0.1(m))^2 = 0.01(m^2)$$

$$A_{1,2} = A_{2,1} = A_{2,3} = A_{3,2} = A_{3,4} = A_{4,3} = A_{4,5} = A_{5,4} = 0.1(m) \bullet 0.0254(m) = 0.00254(m^2)$$

$$h_1 = 150(W/m^2K)$$

$$h_2 = h_3 = h_4 = h_5 = 600(W/m^2K)$$

$$T_{f1} = 294°K$$

$$T_{f2} = T_{f3} = T_{f4} = T_{f5} = 773°K$$

Plugging the values into Eqn. (16) for the first five nodes:

$$T_1 = \frac{\left[\begin{array}{l} 150(W/m^2K)\cdot 0.01(m^2)\cdot 294°K \\ + \dfrac{60.5(W/mK)\cdot 0.00254(m^2)}{0.1(m)}\cdot(T_2 + T_6) + 900(W/m^2)\cdot 0.01(m^2) \end{array}\right]}{150(W/m^2K)\cdot 0.01(m^2) + 2\cdot\left(\dfrac{60.5(W/mK)\cdot 0.00254(m^2)}{0.1(m)}\right)} \quad (17a)$$

$$T_2 = \frac{\left[\begin{array}{l} 600(W/m^2K)\cdot 0.01(m^2)\cdot 773°K \\ + \dfrac{60.5(W/mK)\cdot 0.00254(m^2)}{0.1(m)}\cdot(T_1 + T_3 + T_7) + 900(W/m^2)\cdot 0.01(m^2) \end{array}\right]}{600(W/m^2K)\cdot 0.01(m^2) + 3\cdot\left(\dfrac{60.5(W/mK)\cdot 0.00254(m^2)}{0.1(m)}\right)} \quad (17b)$$

$$T_3 = \frac{\left[\begin{array}{l} 600(W/m^2K)\cdot 0.01(m^2)\cdot 773°K \\ + \dfrac{60.5(W/mK)\cdot 0.00254(m^2)}{0.1(m)}\cdot(T_2 + T_4 + T_8) + 900(W/m^2)\cdot 0.01(m^2) \end{array}\right]}{600(W/m^2K)\cdot 0.01(m^2) + 3\cdot\left(\dfrac{60.5(W/mK)\cdot 0.00254(m^2)}{0.1(m)}\right)} \quad (17c)$$

$$T_4 = \frac{\left[\begin{array}{l} 600(W/m^2K)\cdot 0.01(m^2)\cdot 773°K \\ + \dfrac{60.5(W/mK)\cdot 0.00254(m^2)}{0.1(m)}\cdot(T_3 + T_5 + T_9) + 900(W/m^2)\cdot 0.01(m^2) \end{array}\right]}{600(W/m^2K)\cdot 0.01(m^2) + 3\cdot\left(\dfrac{60.5(W/mK)\cdot 0.00254(m^2)}{0.1(m)}\right)} \quad (17d)$$

$$T_5 = \frac{\left[\begin{array}{l} 600(W/m^2K)\cdot 0.01(m^2)\cdot 773°K \\ +\dfrac{60.5(W/mK)\cdot 0.00254(m^2)}{0.1(m)}\cdot(T_4+T_{10})+900(W/m^2)\cdot 0.01(m^2) \end{array}\right]}{600(W/m^2K)\cdot 0.01(m^2)+2\cdot\left(\dfrac{60.5(W/mK)\cdot 0.00254(m^2)}{0.1(m)}\right)} \quad (17e)$$

Computing the coefficients for the above equations results in:

$$T_1 = \frac{450+1.5367(T_2+T_6)}{4.5734} \quad (18a)$$

$$T_2 = \frac{4647+1.5367(T_1+T_3+T_7)}{10.6101} \quad (18b)$$

$$T_3 = \frac{4647+1.5367(T_2+T_4+T_8)}{10.6101} \quad (18c)$$

$$T_4 = \frac{4647+1.5367(T_3+T_5+T_9)}{10.6101} \quad (18d)$$

$$T_5 = \frac{4647+1.5367(T_4+T_{10})}{9.0734} \quad (18e)$$

Starting with the plate of armor at 300°K, solving Eqn. (18a) for T_1:

$$T_1 = \frac{450+1.5367(600)}{4.5734} = 300°K \quad (19a)$$

Although T_1 remained the same, the new value is plugged into Eqn. (18b) to solve for T_2 (Gauss-Seidel):

$$T_2 = \frac{4647+1.5367(900)}{10.6101} = 568.3292°K \quad (19b)$$

Following the same procedure the new value for T_2 is used for Eqn. (18c) and is repeated for the rest of the nodes:

$$T_3 = \frac{4647 + 1.5367(1168.3292)}{10.6101} = 607.1923°K \tag{19c}$$

$$T_4 = \frac{4647 + 1.5367(1207.1923)}{10.6101} = 612.8210°K \tag{19d}$$

$$T_5 = \frac{4647 + 1.5367(912.8210)}{9.0734} = 666.7547°K \tag{19e}$$

Using a convergence value of $\Delta T = 0.0025°K$ all 25 equations were entered into Matlab and iterated in the same Gauss-Seidel manner until a solution was reached (Matlab file is on the CD that accompanies this report). The solution took 18 iterations to converge using Matlab. The results are shown below in matrix form with node 1 at the top and node 25 at the bottom. Also, the solution to the same problem using MuSES is shown in a graphical form (Figure 14). Both the analytical results and the results from MuSES were the same.

$$T = \begin{bmatrix} 471.7803 \\ 691.1370 \\ 755.1256 \\ 770.1811 \\ 773.3703 \\ 420.1044 \\ 521.0181 \\ 728.4126 \\ 765.1841 \\ 772.1489 \\ 384.7540 \\ 460.1599 \\ 692.3758 \\ 753.6203 \\ 768.7128 \\ 356.7305 \\ 398.8279 \\ 506.6599 \\ 706.6842 \\ 757.7730 \\ 341.9876 \\ 368.2302 \\ 430.4763 \\ 543.8993 \\ 732.6118 \end{bmatrix}$$

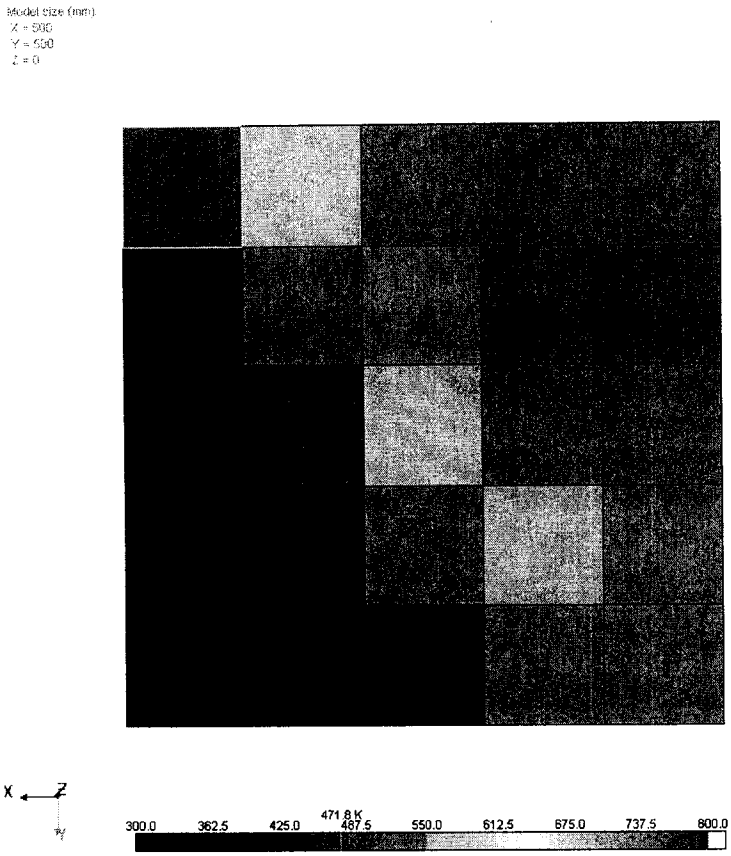

Figure 14. Results from Matlab and MuSES. The results from both the analytical calculations and MuSES were the same.

Thermal Signature Simulation

With the steady state plume characteristics solved for using Fluent, the next step was to setup the thermal analysis in MuSES. For each of the three vehicle variants the surface meshes from Eclectic were imported, and the attributes for the individual parts

were entered. The model consisted of 18009 elements, and 132 parts as shown in Figure 15. All visible parts were painted with Chemical Agent Resistant Coating_Olive Drab (CARC_OD) paint which had an emissivity of .899 and solar absorptivity of .942, except the tires which were treated as rubber. Also, each of the surfaces, except for the tires, were characterized as Steel (mild) 6.45mm thick.

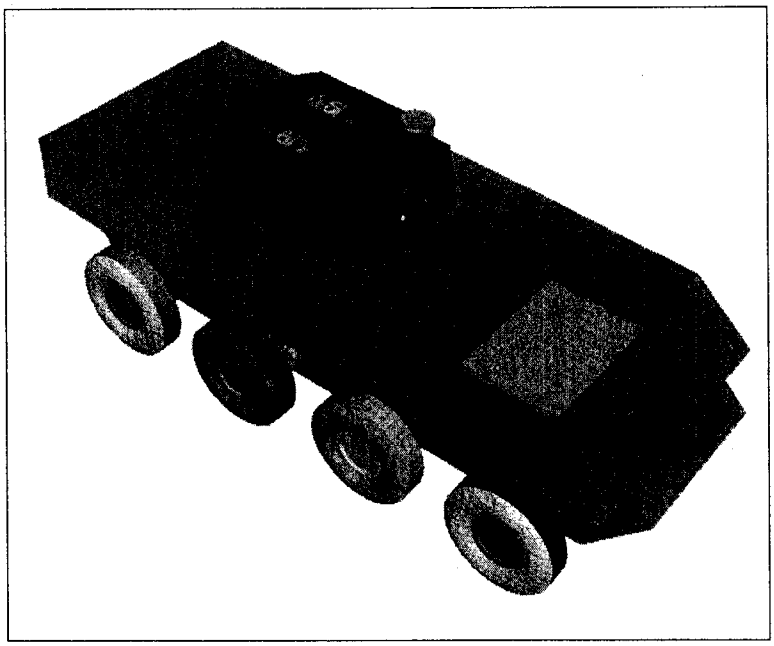

Figure 15. Vehicle geometry used in MuSES.

The environment and the vehicle parameters were entered next. Using weather data that was collected for a previous test (June 27-29, 2002 in Warren, Michigan), the weather file was converted from a Data format (*.dat) to a Prism Weather format (*.wea) so that MuSES could use the file. For this simulation, weather data from June 28, 2002 was used, and the background was set to an Average_Soil setting with a core temperature of 15°C. The vehicle geometry was then positioned to face in the –Y direction, or due

south, so that the bulk of the solar loading would be on the frontal portions of the vehicle. Within the hull, the meshed geometry for the engine was characterized as a Dodge Ram, 24-valve, Turbocharged Diesel V6 using the Engine Parameters portion of MuSES shown in Figure 16. Characterizing the engine allowed for the engine compartment to warm up (radiation and convection) as well as allowing MuSES to calculate an exhaust temperature that was applied to the exhaust outlets via convection. Additionally, for the 20 mph cases the heading (south) and speed were input into the scenario portion of MuSES.

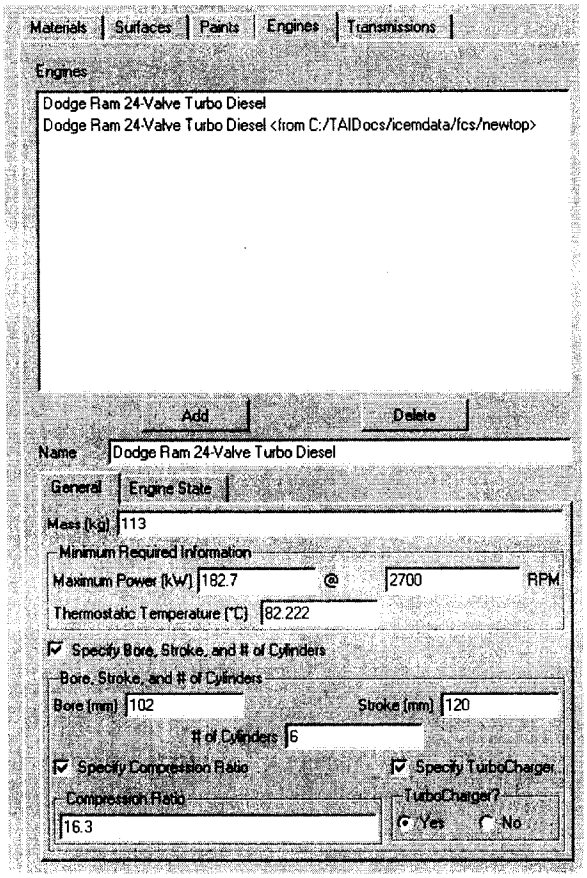

Figure 16. Engine parameter input in MuSES.

The wheels on the 20mph case required special treatment. Physically, all heat loads should be radially distributed across wheels that are rotating. Since MuSES currently does not support that feature, lumped capacitances were used to simulate this case. Each wheel was broken into the following parts: outer wheel, outer tire, tread area, inner tire, and inner wheel. Each part was bound to a lumped capacitance node using very high convection rates to maintain proper mass/heat capacitances and spread the heat loads. The difference in solution is shown below in Figure 17 at 2pm.

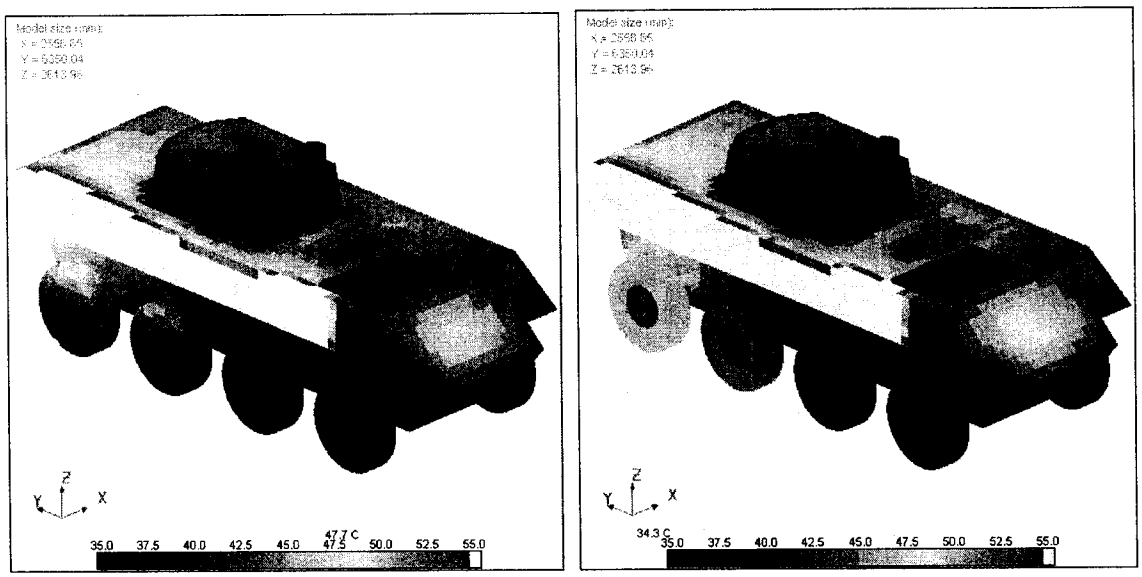

Figure 17. MuSES wheel comparison. Left: 20 mph solution without lumped capacitances to distribute the heat on the rotating wheels. Right: 20 mph solution using lumped capacitances to distribute the heat on the rotating wheels.

Since the exhaust plumes themselves were not that important to this study, but rather the impingement of the plumes on the vehicle, the convection coefficients and film temperatures for the vehicle meshes were imported from Fluent. This way the convection coefficients and film temperatures were applied directly to the nodes within MuSES,

without including the plumes themselves (see Figure 18). Any discrepancy between the meshes was resolved using ThermoAnalytics Inc.'s mesh mapping utility which uses a ray tracer to resolve mesh differences.

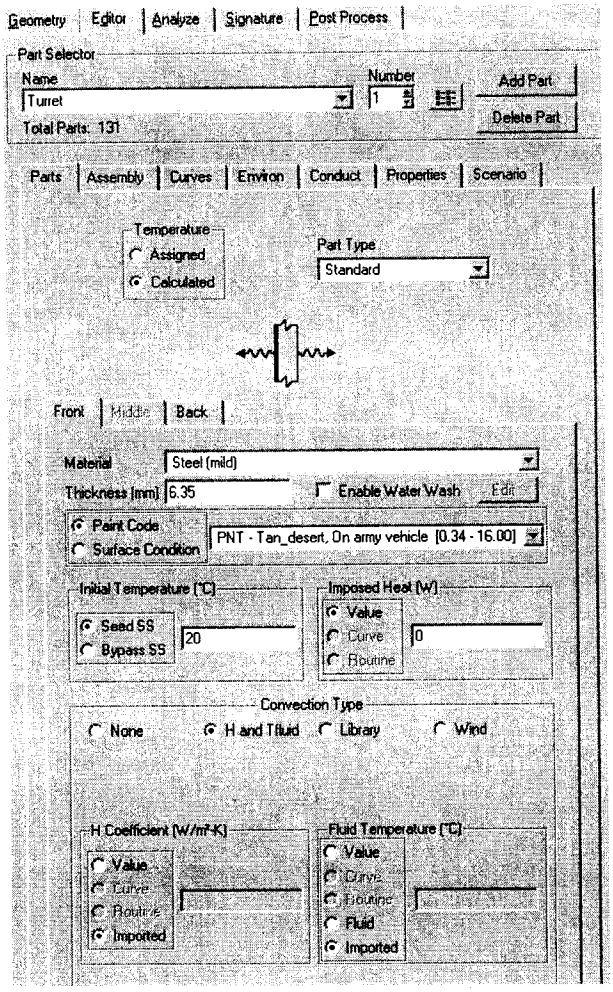

Figure 18. Application of convection in MuSES.

There were some inherent complexities with modeling a steady state plume in CFD and mapping the results onto a MuSES model. The biggest complication came from the fact that the MuSES simulations in a natural environment were transient, while the desired CFD simulation was not. Also, the solutions should have been iteratively

passed between the software packages. The iterative MuSES/CFD solution was not investigated due to time constraints.

MuSES models are typically run for 24 simulated hours prior to the time of interest to come to a cyclic steady state solution. This is to bring all the components to a realistic starting condition in the natural environment. If the CFD boundaries were applied at all the MuSES time steps, the MuSES model would have seen a fixed air temperature and fixed convection on the vehicle resulting in errors. In order to avoid this problem, consider the case of modeling the top exhaust at 20 mph at 2pm. The overall process is shown in Figure 19. The basic MuSES model at 20 mph was run from 5am to 2pm using MuSES' wind convection algorithm. The only heat sources for this step were from the natural environment and the engine heat. The MuSES predicted temperatures were then mapped onto the CFD model and used as wall boundaries. This imposed all of the MuSES heat loads on the CFD model at 2pm. When the CFD solution was solved (the CFD simulation included heated gas from the plume outlet), reasonable convection data was computed on the model for impingement. Impingement data was then exported to MuSES as convection coefficients and film temperatures for each element.

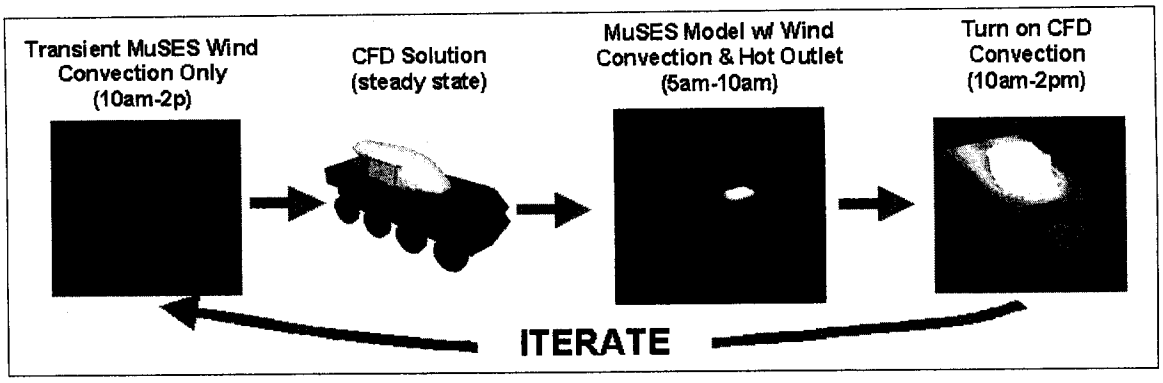

Figure 19. Overall modeling process. Shown is the overall process for achieving a thermal solution. The iteration between CFD and MuSES was not actually performed.

The final step was to run the MuSES model from 5am until 10am with wind convection. Then at 10am, the model was resumed using the imported convection data. Figures 20 and 21 show the temperature convergence of several elements in the plume area over time; this illustrates how quickly the plume affected the solution versus simulation time. It was important to apply the convection of the plume as late in the simulation as possible since it had fixed film temperatures that only matched weather data at 2pm. The idle condition with lower convection and lower temperatures required 4 hours to capture the plume impingement. The 20 mph case with high temperatures and convection coefficients captured impingement within an hour of simulation time.

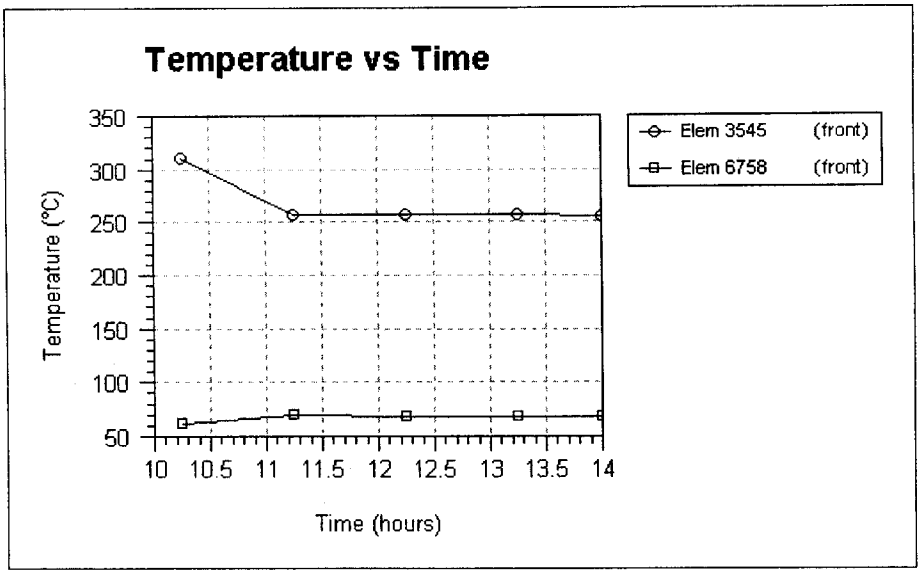

Figure 20. Time to converge for the 20 mph scenario.

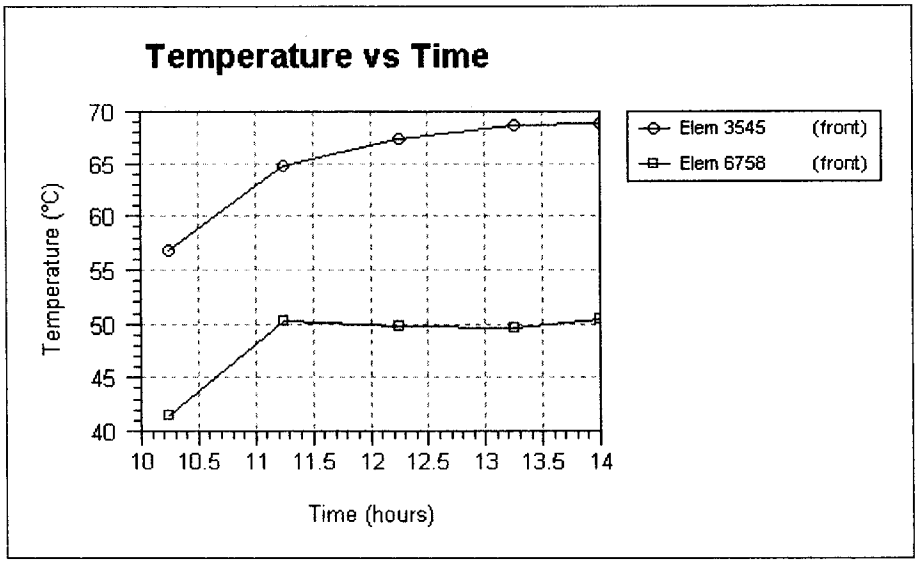

Figure 21. Time to converge for the idle scenario.

After the simulations were completed for each of the scenarios, the thermal radiance for the vehicles was calculated. Using the Signature portion of the MuSES software, the physical temperature outputs for the vehicle meshes converted into radiance

values. Both the 3-5 micron (Mid-Wave) and 8-12 micron (Long-Wave) bands were considered for this application. The end result was a simulated model of the radiance values for the vehicle mesh without taking the viewing angle into account (see Figures 22, 23, 24, & 25).

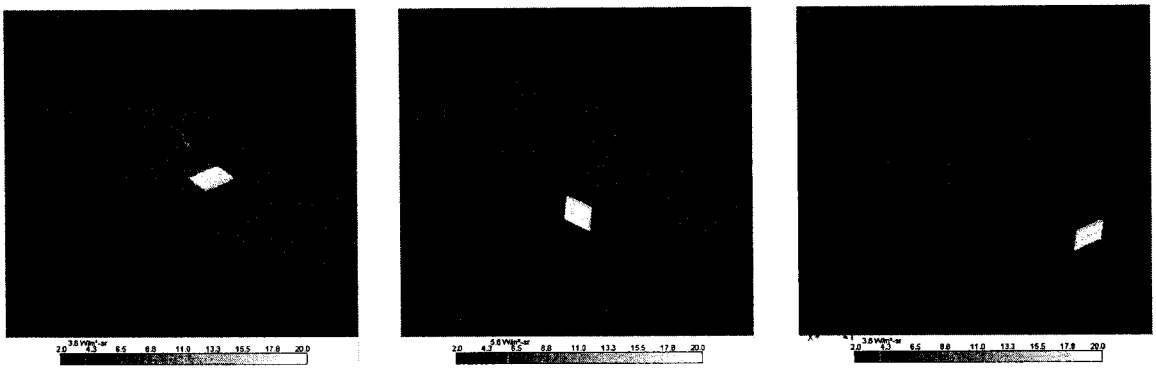

Figure 22. Idle 3-5 micron radiosity solution.

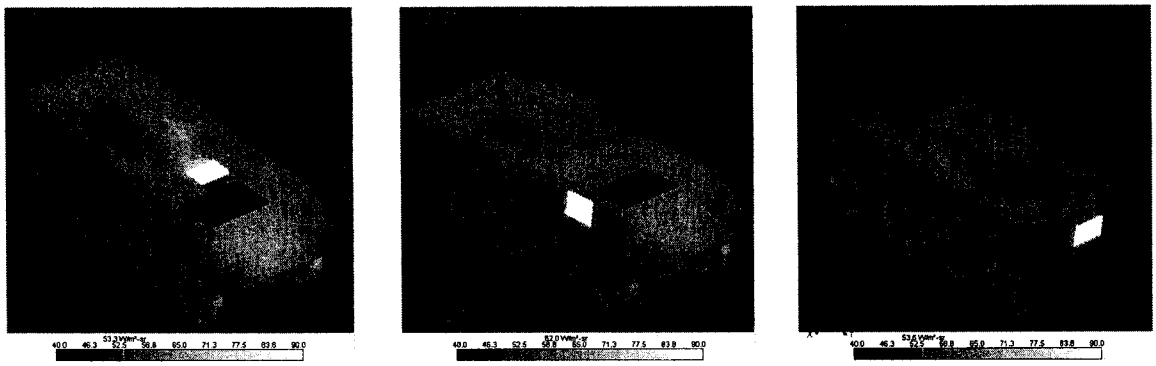

Figure 23. Idle 8-12 micron radiosity solution.

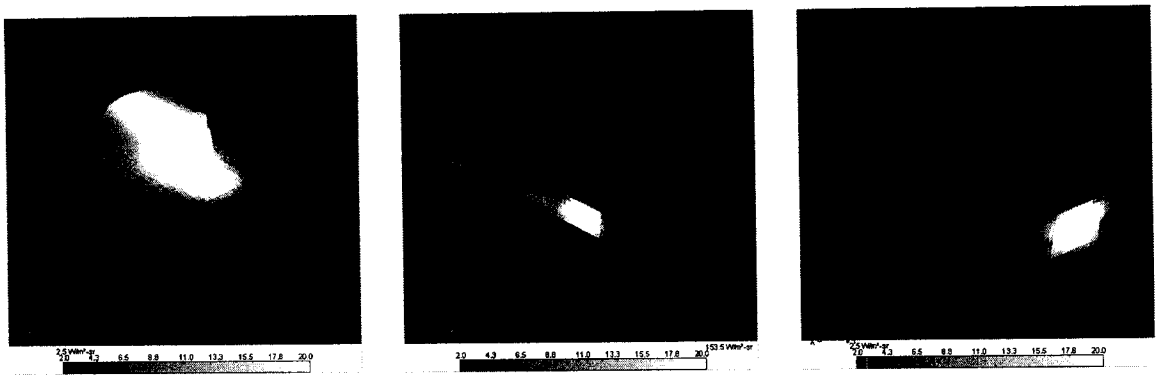

Figure 24. 20 mph 3-5 micron radiosity solution.

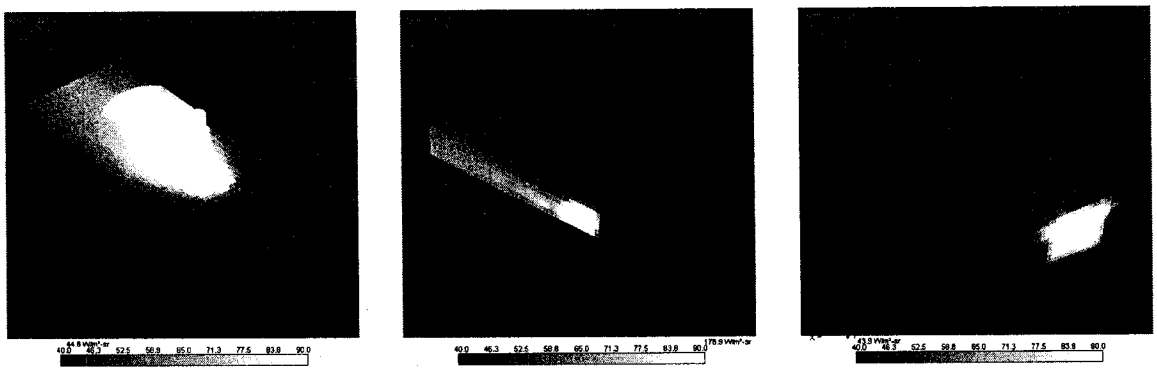

Figure 25. 20 mph 8-12 micron radiosity solution.

Utilizing the Bi-Directional Radiance Distribution Function (BRDF) tool within MuSES allowed for accurate simulated thermal images. While the radiance models were good, they did not take into account thermal reflections due to the viewing angle (i.e. vehicle reflecting itself, solar glints, sky reflections, etc.). By running each of the radiance models through the BRDF package, viewing angles, ranges, and atmospheric effects were applied to the models. What this provided were simulated images of the vehicles, similar to what would be seen through a thermal imager for the selected thermal band (see Figure 26). Unfortunately, the background and foreground within MuSES are represented by a single average temperature that represents the background material

entered by the user. Thus in an actual image one would see the blades of grass, trees, rocks, etc.

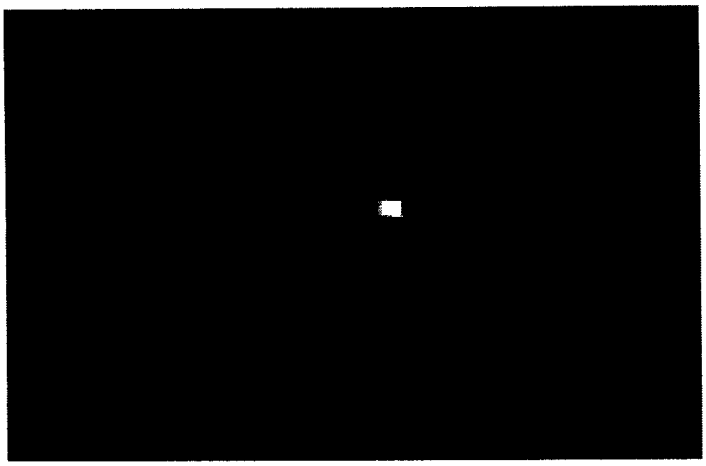

Figure 26. BRDF image of the side exhaust variant.

Along with accurate images, the BRDF tool provided an analysis of each image using the RSSΔT function. RSSΔT is an IR detection algorithm in which the target mean temperature, the background mean temperature, and the standard deviation of the target temperature are all part of the metric. The mathematical representation of this algorithm is:

$$RSS\Delta T = \sqrt{\left(\overline{T}_t - \overline{T}_b\right)^2 + \sigma_t^2} \tag{20}$$

where $\overline{T}_t$ = average target temperature, $\overline{T}_b$ = average background temperature, and σ_t^2 = variance of the target. As the RSSΔT value decreases, so should the probability of detection. Each of the scenarios was then run through the BRDF tool at viewing angle increments of 45°, at an elevation angle of 0°. The range was set to 0.5 km with a FOV

of 0.003°, and a variable depression angle sky model. The RSSΔT values are shown below in Table 2 and Table 3.

Table 2. 3-5 micron RSSΔT values using MuSES.

Viewing Angle	Top (Idle)	Side (Idle)	Rear (Idle)	Top (20 mph)	Side (20 mph)	Rear (20 mph)
0	17.0797	16.4843	16.4739	48.7053	20.4765	4.0676
45	9.1622	11.1385	8.9150	25.9169	43.5583	4.4474
90	6.4479	10.0158	6.6383	16.2814	51.5408	12.5807
135	5.8172	8.6024	8.7508	14.5437	43.0386	45.1396
180	4.2882	5.0704	13.7723	13.3969	18.5597	94.9131
225	6.8449	6.7351	9.5647	14.3673	4.9057	45.3184
270	7.8992	7.8541	8.0923	15.9219	5.0248	12.4232
315	10.2421	9.8164	9.9290	27.6788	4.7103	4.7318
360	17.0797	16.4843	16.4739	48.7053	20.4765	4.0676

Table 3. 8-12 micron RSSΔT values using MuSES.

Viewing Angle	Top (Idle)	Side (Idle)	Rear (Idle)	Top (20 mph)	Side (20 mph)	Rear (20 mph)
0	22.2956	21.7040	21.7013	51.1061	21.8493	4.0331
45	14.9196	16.7180	14.7322	27.9559	45.2523	2.0221
90	12.3104	15.4081	12.5077	18.6656	54.0715	12.9277
135	12.1674	14.3785	14.4825	17.0140	45.1152	46.5619
180	12.3907	12.8206	20.3617	18.7030	20.1853	99.5691
225	13.4228	13.3313	15.6254	16.8212	2.7597	46.7520
270	14.1865	14.1823	14.3911	18.1908	1.2067	12.4633
315	16.2792	15.9024	16.0288	29.8360	1.9470	1.9877
360	22.2956	21.7040	21.7013	51.1061	21.8493	4.0331

Analyzing the results from the RSSΔT study done through MuSES, an idea of what might be the best location for the exhaust outlet emerged. Since viewing angles utilizing a 360° sweep of the vehicle were used, the variant RSSΔT curve that had the least amount of area under it was considered the best. At idle, the top exhaust variant

was the best in both the 3-5 and 8-12 bands, but as shown in the above tables they were all very close (due to the fact that at idle all of the exhaust plumes impinged very little on the hull, but the top exhaust is hidden from a 0° elevation FOV). However, the 20 mph scenario is where the differences in the variants emerged. Looking at Figure 27, there are definite viewing angles that are much better for one variant than another (the 3-5 micron results were very similar to the 8-12 micron results in terms of variant to variant comparison).

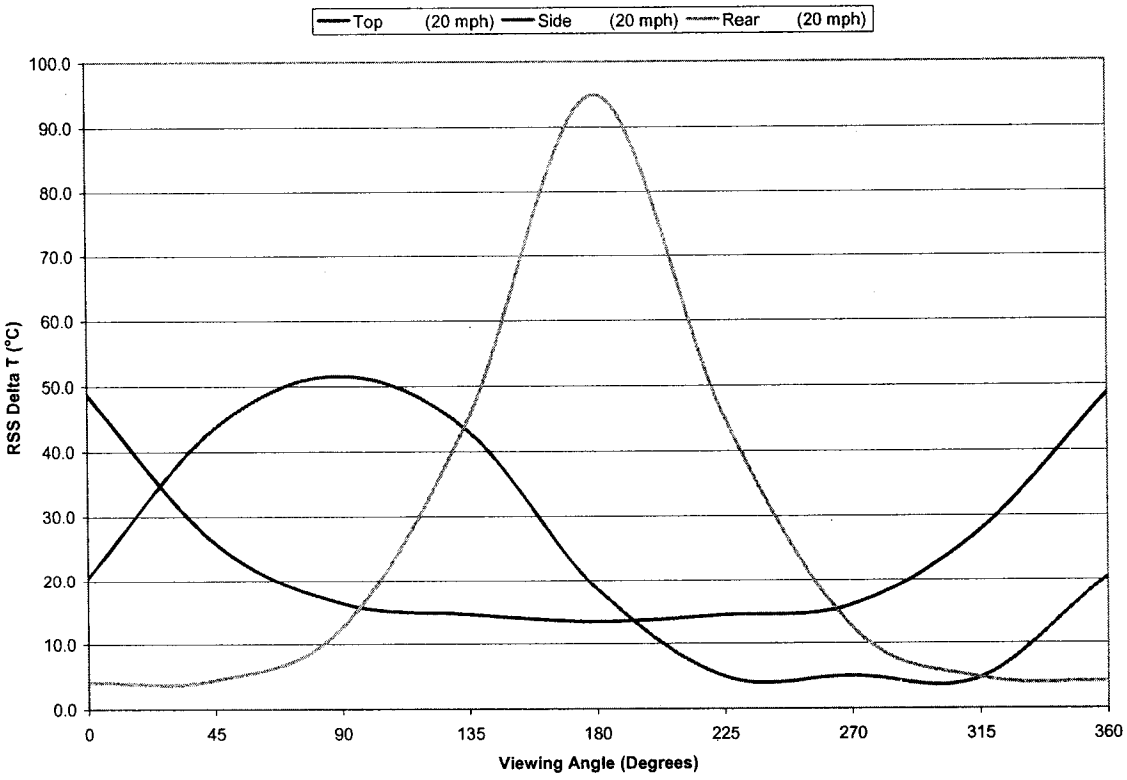

Figure 27. 3-5 micron RSSΔT results.

From a fighting ground vehicle point of view, Figure 27 does not answer the question of which variant has the lowest thermal signature or Pd. To get the final answer

from the simulated results the way in which a formation moves through the battlefield must be taken into account. As discussed earlier, the enemy does not see the rear of the vehicle in battle unless they somehow get behind friendly lines (in which case the thermal signature is the least of their concern). Thermal signatures are treated much like armor, where almost all of the engagement/targeting is taken by the frontal aspect of the vehicle. Hence the focus of thermal signature reduction is focused in this area of the vehicle and not in the rear. Taking an arbitrary conservative approach and only removing the rear 90° of the vehicle RSSΔT curves, the chart in Figure 28 is produced. By taking combat vehicle tactics into account it is plain to see that the rear exhaust location is the clear choice for a minimized thermal signature using the MuSES RSSΔT results.

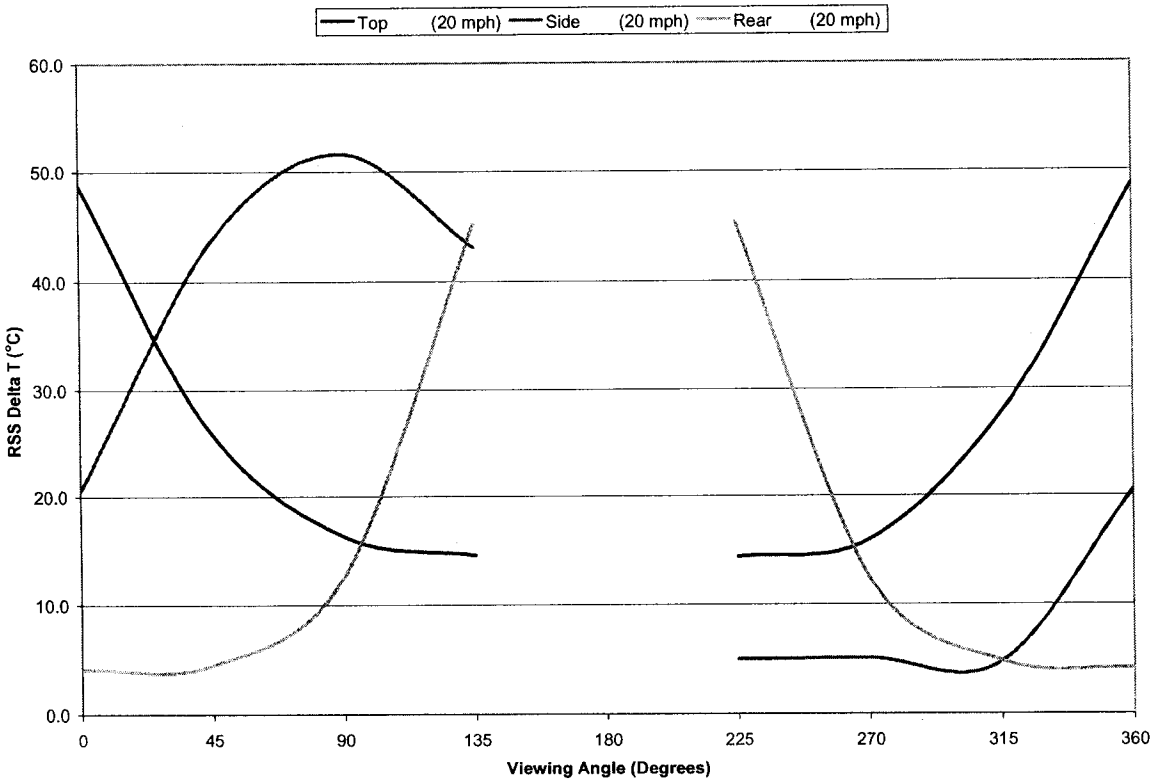

Figure 28. 3-5 micron modified RSSΔT curves.

Pd Analysis

The final simulation used in this study was a thermal perception test performed by Brian Miller of Night Vision Electronics and Sensors Directorate (NVESD). Since the RSSΔT algorithm is used to predict what a soldier would be able to detect at a given range (certain RSSΔT values apply to certain ranges), it only seemed reasonable to compare the findings from the MuSES RSSΔT curves to what a soldier actually detected. Also, since MuSES does not incorporate background objects/clutter such as trees, rocks, grass, or atmospheric interference into its BRDF analysis, applying the variants to a scene with such variables provided data that was closer to the real world.

Two software packages were used to compliment each other for the perception test, CameoSim and Paint the Night (PTN). CameoSim is a scene generating software that was developed by a UK based company named Insys. The objectives for CameoSim were to have an emphasis not on real time capability, but to have the highest order fidelity/physics in both visual and thermal wavelengths. In order to conduct the vehicle studies NVESD created a mock terrain for the US Army TARDEC that provided multiple positions with which to place a vehicle. Figure 29 illustrates a portion of the generated terrain named "Lala-land" after it was imported into CameoSim. A long-wave infrared (LWIR) version of Lala-land was used by PTN for the actual experiments. PTN is a real time capable, thermal image rendering software that was developed by the NVESD at Fort Belvoir. This software allowed for the addition of sensor effects, along with vehicle geometry (also available in CameoSim), multiple targeting scenarios, and the ability to conduction a perception test by selecting possible targets on a video screen. The only vehicle scenario that was utilized for the Pd testing was the 20 mph case.

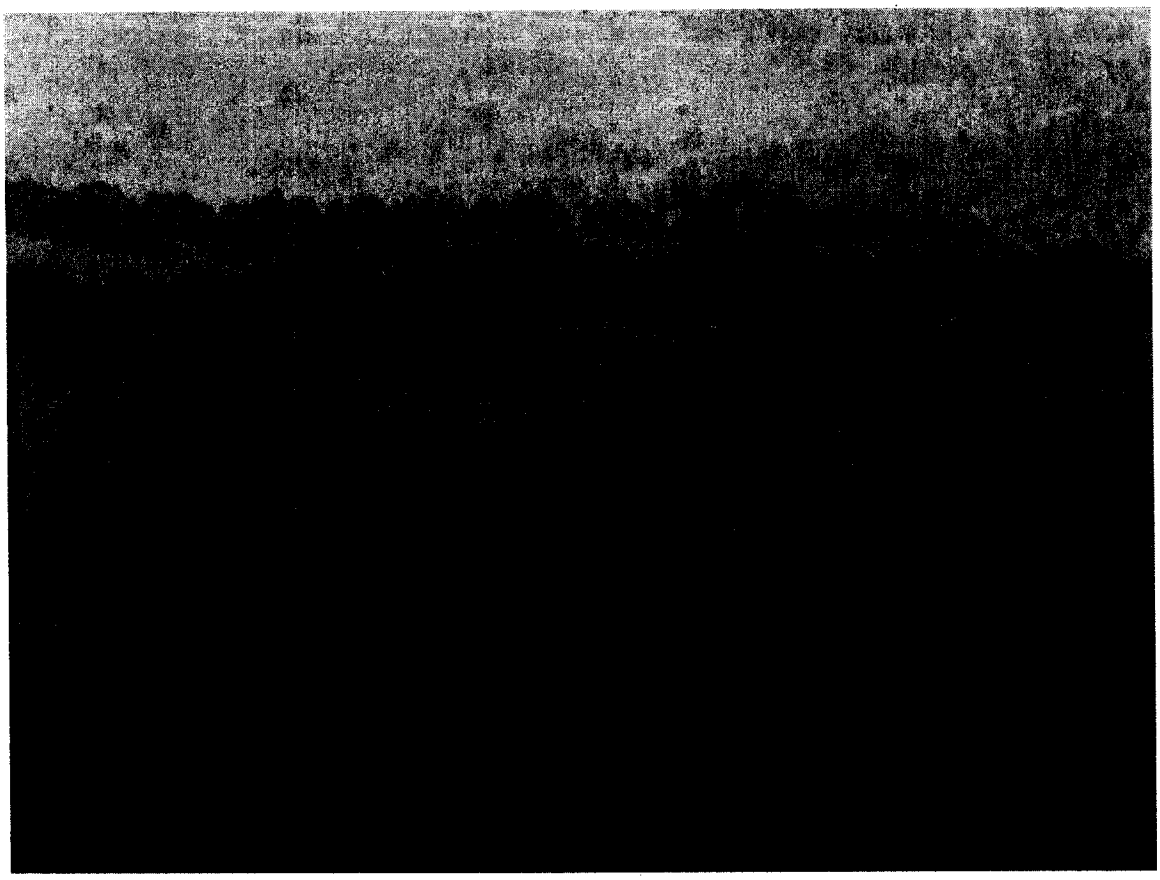

Figure 29. Portion of a simulated terrain from CameoSim.

With the vehicle and terrain geometries input into PTN, the images for the perception test were created. Sixty seven target locations (vehicle geometries being the targets) were determined for forty seven sensor positions on the Lala-land terrain. Images with more than one target position for the sensor position resulted in one of the images being flipped during post processing. Images were generated with each of the three vehicle configurations located in each location at the same aspect, and a no target image. Each image set was post processed with both the first generation and second generation advanced sensor effects.

The set of images were then used in a perception test using actual subjects. The testing consisted of two perception tests, one using modified lower contrast targets and the other using higher contrast targets which were given on consecutive days. Each test had two parts a 1st gen and 2nd gen sensor part, each of which consisted of 200 images. The test was broken into three sets each with only two of the three vehicle configurations and a no target image for each of the positions. Each participant took only one of the sets and was given nine seconds to find the target in the image, or indicate no target by clicking a button. In order to receive results that would reflect what a trained soldier would detect in the field, each of the eight test participants were active-duty soldiers from the 82nd Airborne.

Results from the Pd test contradicted the RSSΔT results. From Figure 30 it is easy to see that using the low contrast vehicle geometries in PTN resulted in the side exhaust being the most difficult to detect. Figure 31 illustrates the same variant having the lowest Pd using the higher contrast vehicle geometries, but the variants are grouped much closer together in terms of Pd (albeit the Pd values are much higher). The reason why the rear exhaust did not favor as well in this study was the fact that all viewing angles were used, so the viewing angles with a rear aspect greatly hindered the Pd of the rear variant (as shown from the RSSΔT curves). Since the contrast values for the targets were modified before the experiment and the backgrounds in the RSSΔT and the Pd analysis were different, any comparison of the results must take this into consideration. With that in mind, in both the RSSΔT and the Pd analysis the top and side exhaust variants were very close to having the same overall signature. However, in the RSSΔT

analysis the top variant was slightly better and in the Pd analysis the side variant was slightly better.

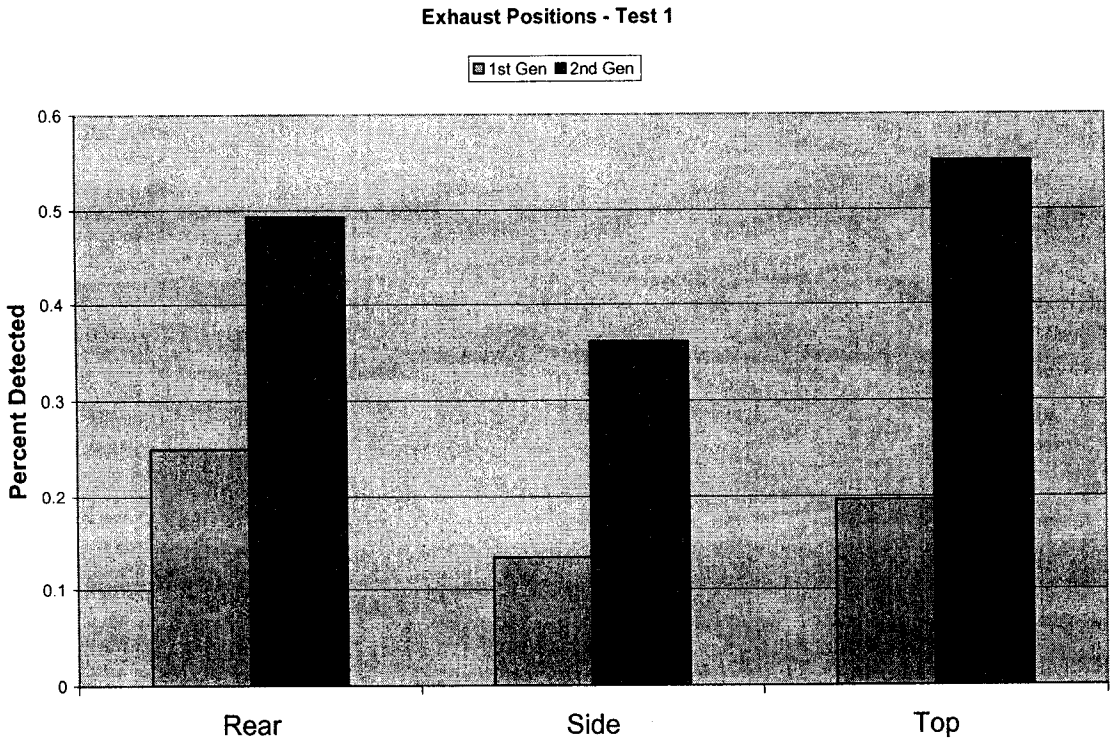

Figure 30. Low contrast vehicle geometry Pd results.

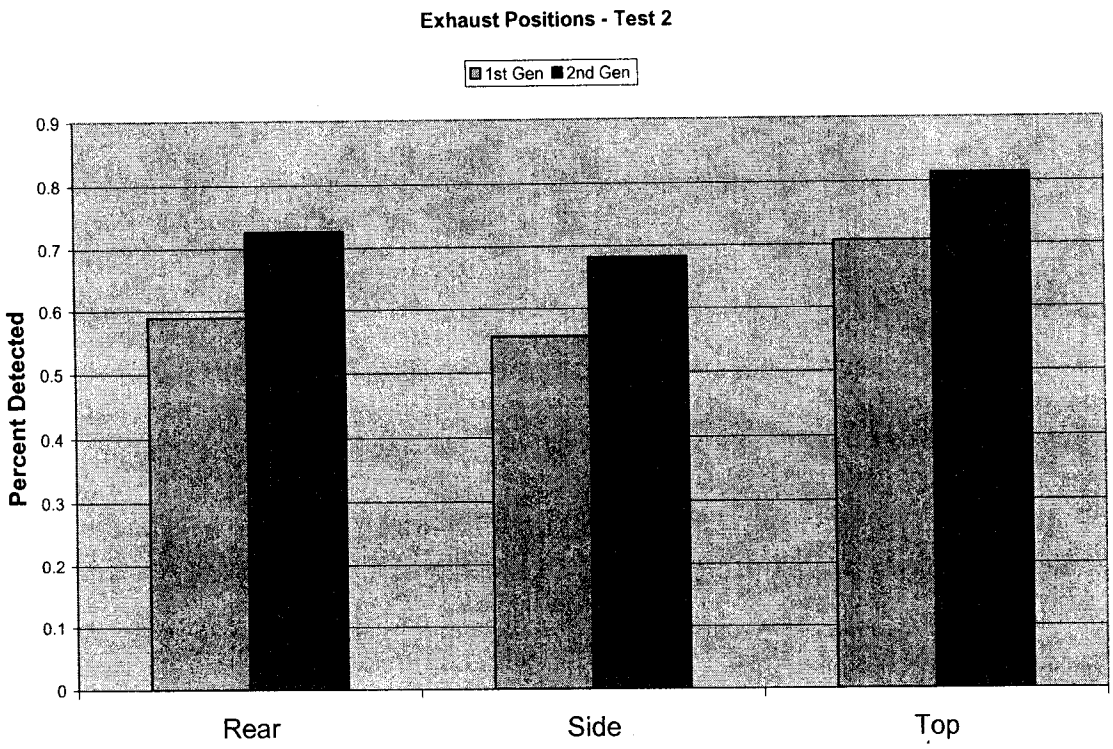

Figure 31. High contrast vehicle geometry Pd results.

Below are some examples of the images used in the Pd analysis. Figure 32 is an example of the low contrast test with a front-right viewing angle, and Figure 33 is an example of the high contrast test with an almost direct rear viewing angle.

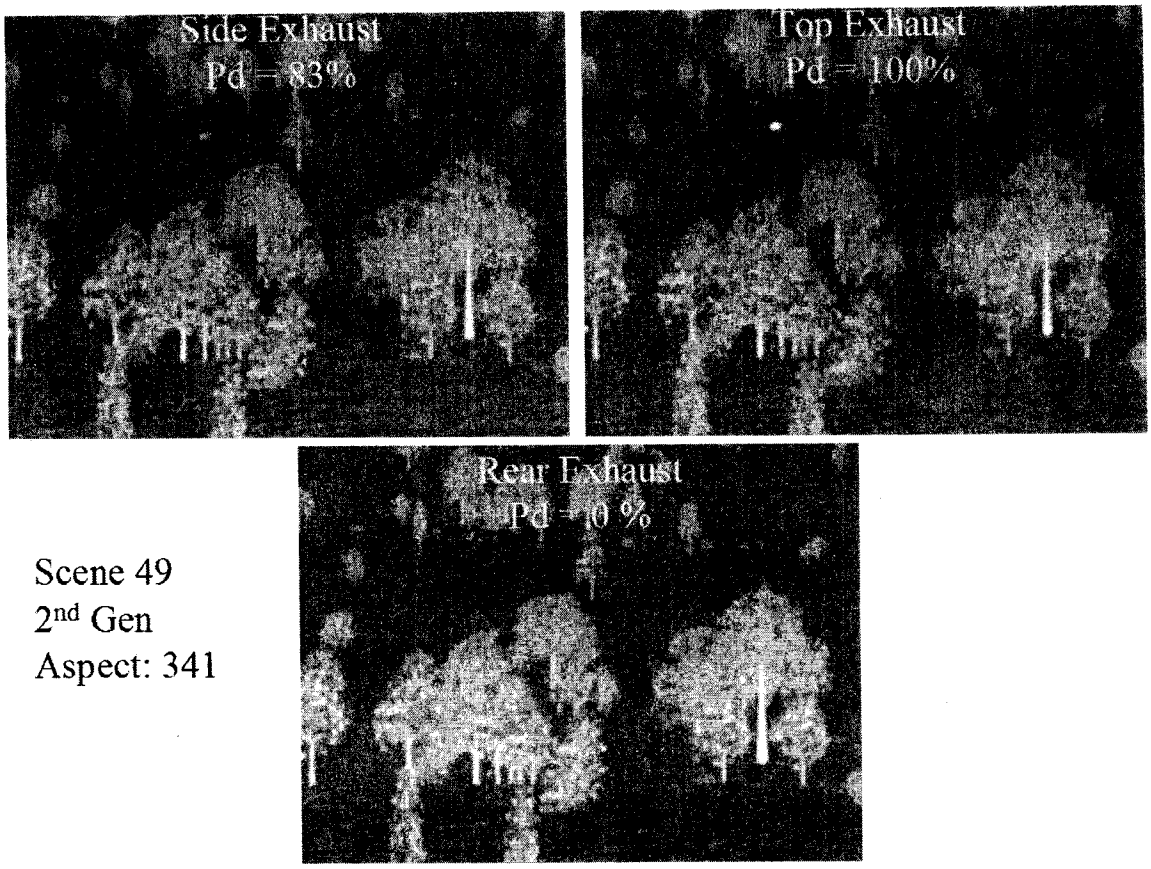

Scene 49
2nd Gen
Aspect: 341

Figure 32. Example of the Pd test 1.

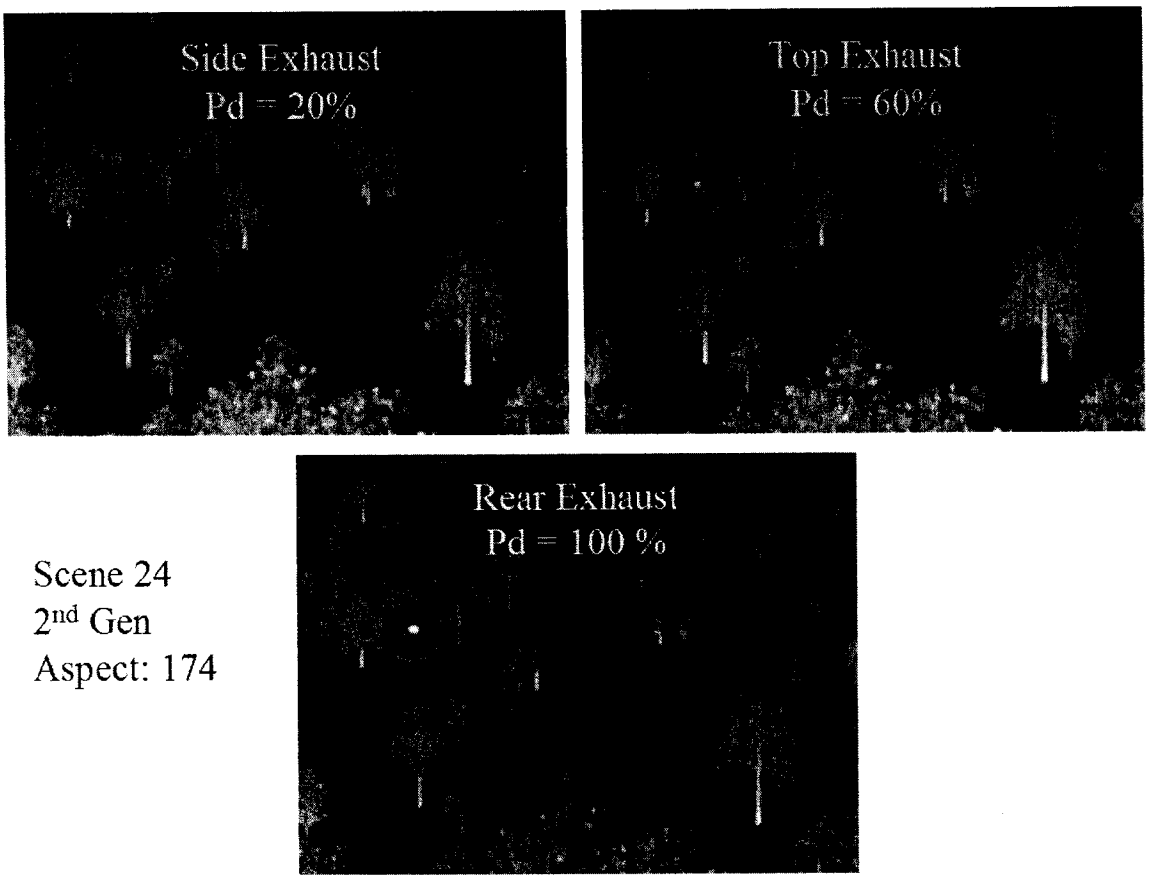

Figure 33. Example of the Pd test 2.

The use of the fluid, thermal, and detection modeling software proved to be invaluable in the analysis of the vehicle exhaust placement. Without the use of simulation tools such as Fluent, MuSES 7.0, and PTN, an un-optimized vehicle design could easily go on to fabrication and production without the realization of the flaw until the vehicle is in service. Finally, although not all of the simulation data was shown in this report, a great deal of the data is included on the CD that accompanied this paper. Also, the complete files are available at US Army TARDEC upon request.